University of Nevada, Reno

Salt-Gradient Solar Pond and Membrane Distillation System for Water Desalination Powered by Renewable Energy

A thesis submitted in partial fulfillment of the
requirements for the degree of Master of Science in
Civil and Environmental Engineering

By

Jeffrey A. Ruskowitz

Dr. Amy E. Childress / Thesis Advisor

December 2012

University of Nevada, Reno
Statewide • Worldwide

THE GRADUATE SCHOOL

We recommend that the thesis
prepared under our supervision by

JEFFREY A. RUSKOWITZ

entitled

Salt-Gradient Solar Pond and Membrane Distillation System for Water Desalination Powered by Renewable Energy

be accepted in partial fulfillment of the
requirements for the degree of

MASTER OF SCIENCE

Amy E. Childress, Ph.D., Advisor

Keith E. Dennett, Ph.D., Committee Member

Andrea Achilli, Ph.D., Committee Member

Scott W. Tyler, Ph.D., Graduate School Representative

Marsha H. Read, Ph. D., Dean, Graduate School

December, 2012

Abstract

A salt gradient solar pond (SGSP) coupled with a direct contact membrane distillation (DCMD) system was investigated to desalinate water for reclamation of Walker Lake, a terminal saline lake in Northern Nevada. Two transparent floating elements and a continuous plastic cover were tested to determine their ability to suppress evaporation rates and increase overall solar pond heat content. An aquatic chemistry analysis was performed on Walker Lake water to determine possible scalants when concentrating lake water to fill the SGSP and during DCMD concentration. Membrane cleaning was evaluated to remove membrane scalant and to recover flux.

It was found that petri dishes were the best evaporation suppression element due to their transmissivity, low refraction of radiation, and ease of installation. Suppression of evaporative losses from the solar pond surface also resulted in increased temperatures throughout the solar pond and increased overall solar pond heat content. The investigation of transparent covers/elements is unique from previous studies in ponds where increasing temperature and heat content are not desired.

Hydromagnesite and calcite were predicted to form during concentration of Walker Lake water to fill the SGSP. Hydromagnesite and halite were found to be the main scalants on the membrane surface. Halite most likely formed due to concentration polarization at the membrane surface; small quantities of calcite were also likely present although not detected. Cleaning cycles were conducted and were able to recover approximately 94% of the original flux using citric acid or EDTA

cleaning solutions. The citric acid cleaning solution performed slightly better than the EDTA cleaning solution in terms of flux recovery and removal of scalant (as observed by SEM). SEM, EDS, and XRD analyses were performed in order to determine the magnitude of scale deposit and the type of scalant present.

The proposed coupled SGSP/DCMD system was found to be feasible for terminal lake reclamation when utilizing floating elements to suppress evaporation and cleaning cycles to remove membrane scale and restore flux across the membrane. Positive freshwater production rates from the coupled SGSP/DCMD system, which have not been achieved in previous coupled systems, were achieved in this investigation.

Acknowledgements

I would like to express my sincere gratitude to my advisor Dr. Amy Childress. I would not be where I am in my academic career without her constant support, advice, and inspiration. She provided me with a great opportunity as an undergraduate student to work with many talented researchers on a variety of interesting projects. The lessons I learned from this work carried me through my graduate studies and will stay with me through my future interests and professional career.

I would also like to thank the other members of my committee: Dr. Keith Dennett, Dr. Scott Tyler, and Dr. Andrea Achilli. Their mentoring, teaching, and questions shaped my project and this thesis into what it is today.

I owe many thanks to Dr. Francisco Suarez; his help and advice over the last 5 years was tremendous. Dr. Sage Hiibel, if even for a short time, directed me towards answers that were not immediately apparent, unless it was 3.

I also wish to thank my colleagues in the Civil and Environmental Engineering Department, who have managed to keep me sane for the last 5 years. A special shout out goes out to Jeri Prante and also Katie Bowden and Guiying Rao of the Childress Membrane Research Group.

Finally, I thank my family: my sister, Emily, and my parents, Dave and Susie. Without their constant support I would not be where I am today.

Table of Contents

List of Acronyms

MD	Membrane distillation
SGSP	Salt gradient solar pond
DCMD	Direct contact membrane distillation
RO	Reverse osmosis
MSF	Multi-stage flash
MED	Multiple-effect distillation
EDTA	Ethylenediaminetetraacetic acid
UCZ	Upper convective zone
NCZ	Non-convective zone
LCZ	Lower convective zone
AGMD	Air gap membrane distillation
SEM	Scanning electron microscope
EDS	Energy dispersive spectrometry
XRD	X-ray diffraction
DTS	Distributed temperature sensing
PETG	Polyethylene terephtalate glycol
PTFE	Polytetrafluoroethylene

List of Figures

List of Tables

1. Introduction

1.1 Terminal lakes

Terminal lakes are often found in desert regions and are in a stage of long-term equilibrium where the inflows (precipitation, groundwater discharge, and stream and river runoff) are equal to the outflows (groundwater discharge and surface evaporation) [1]. Throughout the years, inflows from streams and rivers are often reduced by various uses upstream from the terminal lake. These diversions result in a drop in water elevation and an overall reduction in lake storage. Because the only outflows that exist from the lake are groundwater discharge and surface evaporation, most deposited salts and other constituents remain trapped in the lake. Therefore, overall salt concentration increases over time [2].

Over the past 100 years, Walker Lake, a terminal lake located in western Nevada, has experienced a steady decline in lake elevation and an increase in total dissolved solids (e.g., sodium, magnesium, chloride, and alkalinity) (Figure 1) [3]. These effects have been magnified as inflows to the Lake, such as the Walker River, are diverted for agricultural and other uses. As much as 75% of the Walker River is diverted for agricultural uses [4]; this has caused the lake surface elevation to drop nearly 150 feet in the last 130 years [5] and the concentration of total dissolved solids to increase nearly 700% from 1882 to 2008 [5]. The changing conditions in Walker Lake has harmed fish species (e.g., forage fish and tui chub) and other biological diversity (e.g., algae, zooplankton, and microorganisms) and entirely eliminated the Lahontan cutthroat trout [4-6].

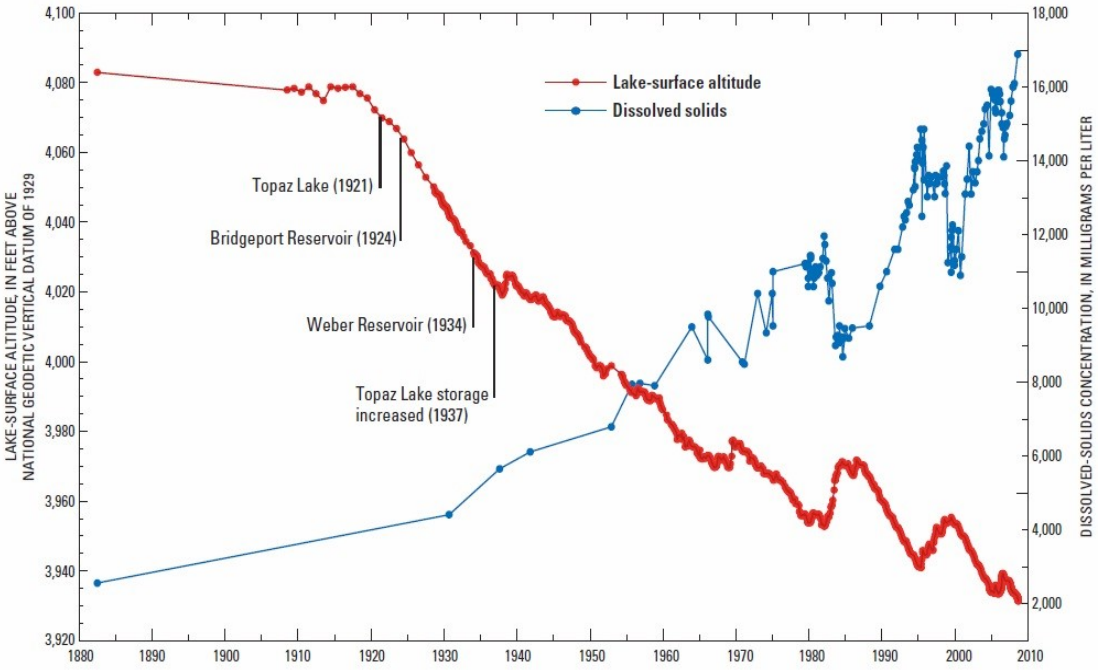

Figure 1: Walker Lake surface elevation and total dissolved solids from 1882 to 2008. Figure taken from Lopes et al. [5].

In order to increase lake surface level and decrease salt concentration, a desalination system that can remove salt from the lake water could be implemented. Additionally, the locations of terminal lakes may necessitate the use of remote means for energy collection and storage. Membrane distillation (MD) is a thermally driven desalination process that can be easily coupled to a renewable energy source, such as solar energy [7]. Whereas some solar energy collection devices, such as photovoltaics, have high capital costs [8], a salt gradient solar pond (SGSP) may provide low-cost solar energy collection and storage. SGSPs can also be operated at minimal cost and minimal operational maintenance for long periods of time [9], making them ideal solar energy capture devices in remote locations. Coupling an SGSP with a direct contact membrane distillation (DCMD) system provides a synergistic means for reducing salinity in terminal lakes.

1.2 Membrane distillation for water desalination

MD utilizes a hydrophobic, microporous membrane that allows evaporation of a volatile solute or solvent through the membrane pores when there is an induced vapor pressure difference through the membrane [10]. In DCMD, a higher temperature feed stream is in direct contact with the active side of the membrane and a lower temperature distillate stream is in direct contact with the support side of the membrane. This temperature difference results in a vapor pressure difference across the membrane [11]. The higher temperature stream loses water through evaporation through the hydrophobic, microporous membrane and this vapor condenses directly into the lower temperature stream, resulting in a freshwater flux [12].

MD does not require the high operating pressures that reverse osmosis (RO) requires and does not require the high operating temperatures that multi-stage flash (MSF) distillation and multiple-effect distillation (MED) require [13]. The effect of higher salt concentrations on MD is minimal, as vapor pressure is only marginally decreased with increasing concentration [14]. Another advantage of MD is the rejection of nonvolatile solutes or solvents, resulting in nearly 100% rejection of salts and a very high quality distillate [15, 16]. Therefore, waters that include constituents at high concentration factors (even at or near supersaturation) may be successfully treated with MD. Additionally, the increased recovery that results from high concentration operation of MD decreases the volume of concentrated brine that needs to be disposed of after treatment [17, 18]. In MD, and DCMD more specifically, only a low-grade heat source and two low power pumps for recirculation of the feed and distillate loops are required.

1.3 Energy collection and storage

As solar radiation penetrates into a body of water (e.g., a lake or pond), the warmed water rises to the surface as a result of decreased density. Once this warmed water reaches the surface, heat is easily lost to the atmosphere through evaporative cooling. This heat loss is magnified at night due to higher heat transfer into the cooler atmosphere [19]. An SGSP is specifically designed to inhibit the rise of warm water and the loss of heat to the atmosphere through the use of a salinity gradient.

An SGSP (Figure 2) consists of three distinct thermal zones: an upper convective zone (UCZ), a non-convective zone (NCZ), and a lower convective zone (LCZ). The UCZ is the uppermost layer in the pond and consists of fresh or lower salinity water that is in contact with the air above it and the NCZ below it. The NCZ consists of an increasing salinity gradient with increasing depth that acts as insulation to the LCZ below. The LCZ, located in the deepest section of the solar pond, contains the most saline (and thus most dense) solution. This lowest zone also contains the highest temperatures in the solar pond. Mixing occurs inside both the UCZ and LCZ due to the constant water density that exists in these two zones. However, the concentration gradient in the NCZ inhibits whole-pond mixing. If mixing occurs in this zone, the pond would lose the ability to store heat in the LCZ [20]. As radiation penetrates into the solar pond through the UCZ and NCZ and into the LCZ, the water is warmed. This warmed water is trapped in the LCZ because of the water's higher density than the NCZ above. Previous studies have shown LCZ temperatures can reach as much as 110 °C, with a maximum difference in temperature between the UCZ and LCZ of 70 °C [21, 22].

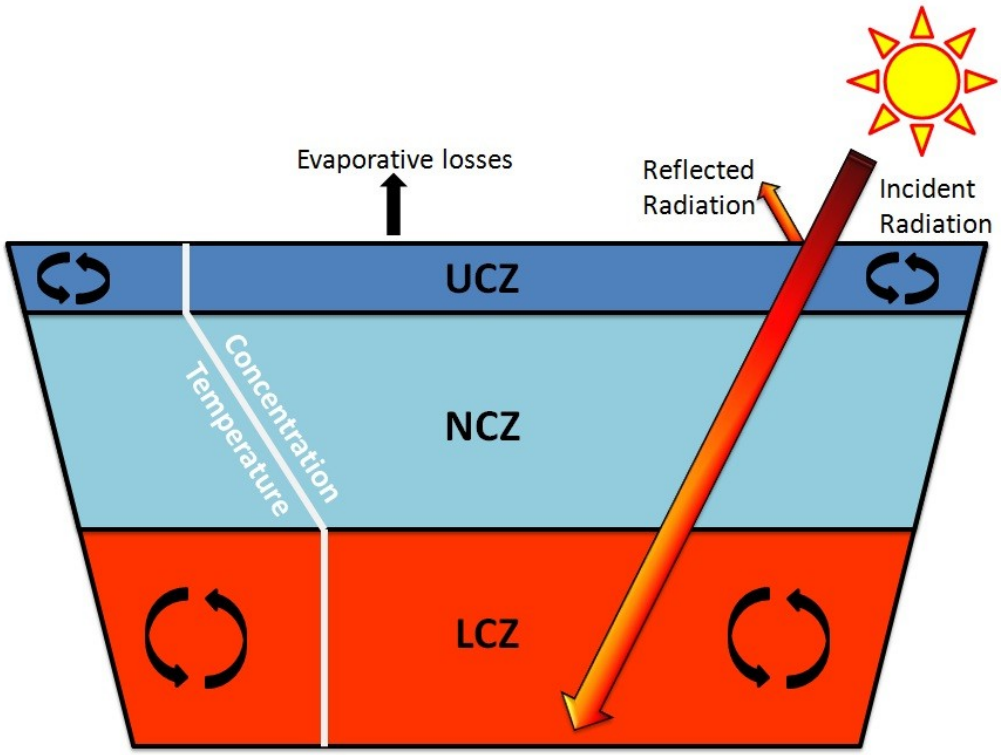

Figure 2: A salt gradient solar pond (SGSP) schematic. Solar radiation that penetrates through the UCZ and NCZ is stored in the LCZ. A temperature gradient forms in the NCZ that mimics the concentration gradient in the NCZ.

Near year-round operation of SGSPs has been proven successful with very little maintenance [23-27]. In the northern hemisphere, spring and summer are the peak seasons for solar radiation collection [28], although solar pond operation in both fall and winter seasons is still entirely possible [23]. The average measured solar radiation over a year for a collection site in Reno, NV is shown in Figure 3 [29]. The peak collection is during the month of July, when average solar radiation is greater than 11 kWh per m^2 per day. The lowest months of radiation are from November through February, when average solar radiation is less than 6 kWh per m^2 per day. When operating an SGSP during months of less solar radiation, heat extraction has to

be more carefully managed as the effects of heat extraction on the stability of the solar pond become increasingly important [30].

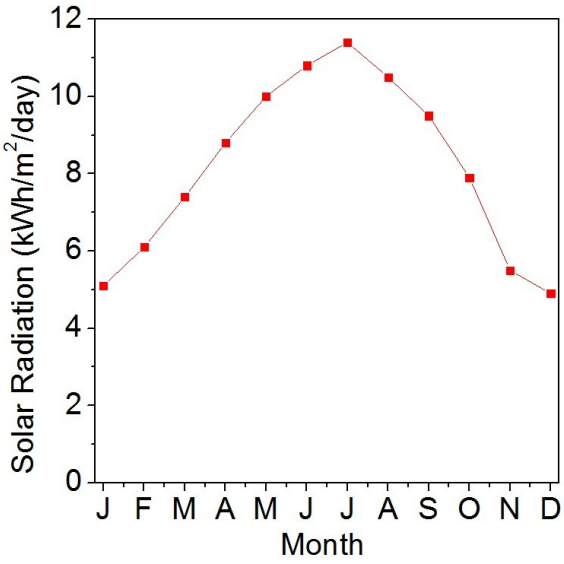

Figure 3: Average daily solar radiation in Reno, NV. Measurements were made using a two-axis flat plate collector.

Thermal energy in the form of radiation reaches the earth in the form of shortwave radiation from the sun [31]. There are three distinct types of shortwave radiation, near-ultraviolet, which occurs from 10 to 390 nm; visible, which occurs from 390 to 750 nm; and near-infrared, which occurs from 750 to 1000 nm. As a water body collects shortwave radiation, the temperature of the water body increases and the emission of temperature-dependent longwave radiation increases. Longwave radiation emitted from the surface of solar ponds results in a loss of temperature and a decrease in overall solar pond efficiency [32]. This effect, which results in cooling of the solar pond surface, is magnified during night time operation.

1.4 Previous SGSP/DCMD experimental work

The SGSP/DCMD system at the University of Nevada, Reno (UNR) was previously tested as reported by Suarez et al [33]. A high temperature of 34 °C was achieved in the LCZ with 12-hour light/12-hour dark cycles. Heat was extracted from the solar pond and pumped through a heat exchanger. The other stream through the heat exchanger was freshwater feed from a hollow fiber DCMD membrane module. Modeling of this system showed that production of 2.70×10^{-3} m^3 of freshwater per day per m^2 of solar pond surface area was theoretically possible [1]. An experimental water production of 1.16×10^{-3} m^3 of freshwater per day per m^2 of solar pond surface area was achieved with the system operating at non-steady state conditions [1]; that is the pond needed time for temperature recovery in the LCZ after 40 hours of operation. However, evaporative losses from the solar pond surface were higher than both the actual and predicted water production values.

An outdoor solar pond in El Paso, Texas was previously studied for heat extraction [25, 27]. A maximum water production of 0.16×10^{-3} m^3 of freshwater per day per m^2 of solar pond surface area was obtained when the solar pond was coupled with an air gap membrane distillation (AGMD) system [25]. AGMD traditionally has lower flux than DCMD [34]. The feedwater was pure water and a 41 °C temperature difference was measured across the membrane. Evaporative losses were not considered in that study.

These previous studies indicate that evaporation suppression from the solar pond surface is necessary to provide positive net freshwater production. Two possible solutions for evaporation suppression were given by Suarez et al. [1]: 1) to construct

the solar pond inside the terminal lake so as to not increase the surface area available for evaporation, or 2) to suppress evaporation from the surface of the solar pond directly. Suppressing evaporation from the solar pond surface may be a simpler solution than constructing a solar pond inside the lake itself. When evaporation is suppressed from the surface of a solar pond, heat loss from the surface decreases [35]. Heat loss through the side walls and bottom of a large solar pond can be considered negligible when compared to evaporative heat losses from the surface of the solar pond [36]. Therefore, evaporation suppression would also likely result in an increase in temperature throughout the solar pond, therefore improving the overall efficiency of the SGSP/DCMD system [1, 33].

1.5 Evaporation suppression

During operation of a solar pond, evaporative losses become a significant problem when limited water sources are available for replenishing the UCZ, as in the case of terminal lake reclamation. Several different methods can be considered to suppress evaporative losses from water bodies.

The use of shading materials for evaporation suppression has previously been studied [37, 38] and these studies were focused on the suppression of evaporative losses without the need for retaining or increasing heat inside the water body. These studies utilized opaque covers/elements, whereas in solar pond studies, transparent covers/elements would be desired. In one study, reduction in evaporative losses up to 80% was achieved by completely shading the water surface [37]. One of the more recent studies was carried out by Assouline et al. and focused on the suppression of

evaporative losses using partial covers [38]. However, temperatures through the water volume were not considered, nor were the covers selected for radiation penetration properties. It was found that the size and spacing of openings in a non-transparent polypropylene sheet installed over a water surface were important factors for the reduction of evaporative losses [38]. Therefore, certain designs and geometries of partial covers can increase the water surface to air contact ratio and could actually increase evaporative losses. The ideal cover type should be designed for a large surface area to perimeter ratio in order to effectively suppress evaporation from solar pond surfaces.

All previous studies, which were focused on shading of the water surface, will result in a decrease in radiation that reaches the solar pond surface, thereby decreasing the temperature throughout the water column. Due to the reduction or blockage of the penetration of solar radiation, these opaque cover types are not useful for suppression of evaporation from the surface of an SGSP. On the other hand, transparent evaporation suppressers (e.g., continuous plastic covers or floating elements) could reduce evaporative losses and increase useable heat in the solar pond. Continuous plastic covers have been used for years to reduce evaporation from pools and increase overall pool water temperatures. Theoretically, continuous plastic covers can completely eliminate evaporative losses from a water surface. In comparison, transparent floating elements offer ease of installation, transparency, and the ability to be retrofitted to existing solar ponds. An added benefit of covering the surface of the solar pond is the reduction of wind-driven mixing.

1.6 Effects of salinity and scaling on solar pond and MD system

When concentrating Walker Lake water to fill the dense LCZ and the salinity gradient of the NCZ, salt precipitation is possible. These precipitants could increase the turbidity of the water column in the solar pond, which could cause the solar radiation that penetrates through the surface of the solar pond to be reflected back out of the solar pond before reaching the storage zone (LCZ). Through development of an empirical correlation between water turbidity and the penetration of solar radiation into the water column, it was shown that the negative effect of turbidity on radiation penetration increases as the depth of the water column increases [39]. Thus, turbidity could decrease thermal storage and overall thermal efficiency [40-43]. Therefore, analysis of precipitants that could form in the water column is critical to ensuring the most efficient operation of an SGSP.

The precipitate that forms while concentrating Walker Lake water to prepare the LCZ and NCZ would also likely be the same precipitate that forms on the membrane surface when Walker Lake feedwater is concentrated in DCMD. There are two distinct ways that scale can be deposited or formed on the membrane surface: 1) higher concentrations, that reach saturation, can lead to precipitates forming upstream of the membrane surface resulting in deposition of scale on the membrane surface [44], and 2) scale can form directly on the membrane surface from the vaporization of water across the membrane [45]. Additionally, increased precipitation near the membrane surface as a result of temperature polarization [46] and concentration polarization phenomena [47, 48] can increase the likelihood of membrane scaling. Concentration polarization can also result in the formation of scale in the bulk at

conditions below saturation [49]. For example, halite (NaCl) is highly soluble in water but has been shown to precipitate from solutions when only a slight loss in water volume occurs [50].

1.6.1 Results from unpublished literature on related investigations

CHEMCHAU is an equilibrium chemical thermodynamic model [47] that utilizes the PITZER equations [51] and can be used from 25 to 100 °C, which is necessary for modeling Walker Lake water concentration in a solar pond. CHEMCHAU is parameterized for the Na-K-Mg-Ca-H-Cl-ClO_4-SO_4-OH-CO_3-CO_2-O_2-CH_4-Si-H_2O system and can evaluate the precipitation of solids such as calcite ($CaCO_3$) and hydromagnesite [$Mg_5{\cdot}(CO_3)_4{\cdot}(OH)_2{\cdot}4H_2O$]. In an unpublished study [52], the CHEMCHAU model was used to predict the precipitants and scalants that would likely form during the concentration of Walker Lake water. The model was also used to provide the percent concentration that Walker Lake water must be concentrated to provide the dense waters required for the LCZ and NCZ in the solar pond.

Walker Lake solution chemistry data was used as input for the model [3]. The composition of Walker Lake as reported in Collopy and Thomas [3] in units of g per L and units of mol per kg of water that were required for input into the CHEMCHAU model [47] is presented in Table 1. According to model calculations and prior to concentrating the water, Walker Lake water is supersaturated with respect to both calcite and hydromagnesite. The CHEMCHAU-predicted composition of the Walker Lake water after being reduced to 10% of its original volume (90% concentration),

which was required to form the LCZ, is also presented in Table 1. Concentration of the water causes most components to significantly increase in concentration, except for Ca^{2+} and Mg^{2+}, which precipitate out of solution immediately.

Table 1: Chemical composition of Walker Lake water [4] and Walker Lake water that was concentrated by 90% at a temperature of 80 °C.

	Walker Lake		Walker Lake Concentrated to 90%	
Constituents	**g/L**	**mol/kg (H_20)**	**g/L**	**mol/kg (H_20)**
Na	5.0400	0.2271	50.4420	2.2728
K	0.2700	0.0070	2.7020	0.0696
Ca	0.0103	0.0003	0.0004	0.0000
Mg	0.1890	0.0078	0.0065	0.0003
Cl	3.5290	0.1001	35.3180	1.0022
SO_4	3.5700	0.0374	35.7290	0.3741
alkalinity	3.4580	0.0753	27.2090	0.5925
pH	9.37	9.37	9.84	9.84

Solubility data for possible precipitates from the concentration of Walker Lake water is shown in Table 2. Significant precipitation of calcium carbonates, such as calcite, and magnesium carbonates, such as magnesite ($MgCO_3$), dolomite [$CaMg(CO_3)_2$], and hydromagnesite, in high pH solutions (9.37-10.23) is typical [47].

Table 2: Solubility data for precipitates expected to form during the construction of an SGSP with Walker Lake water. (*Closest available data found to 20 °C)

Species	Solubility (g/100 g Water)	Temp (°C)
$CaCO_3$ *(Calcite)*	0.006	20
$MgCO_3$ *(Magnesite)*	0.040	20
$CaMg(CO_3)_2$ *(Dolomite)*	0.003	17*
$Mg_5(CO_3)_4(OH)_2.4H_2O$ *(Hydromagnesite)*	0.076	25*
NaCl *(Halite)*	35.890	20
Na_2CO_3 *(Soda Ash)*	21.500	20
Na_2SO_4 *(Thenardite)*	19.500	20*
KCl *(Potash)*	34.200	20

Up to 99.03% concentration of Walker Lake water was modeled at temperatures of 60, 80, and 100 °C. Mineral compositions were minimally influenced by changes in temperature, so only data from the 80 °C case was considered. Complete 100% concentration was not achieved; the model was unable to converge above 99.03% concentration. Figure 4 shows CHEMCHAU model predictions for concentrating Walker Lake water to 99.03% at 80 °C. Arrows point to the start of mineral precipitation for this aquatic system. Throughout the entire concentration process, magnesium and calcium were both at low concentrations and did not increase due to constant precipitation of carbonate (CO_3^{2-}) salts in the form of hydromagnesite and calcite, respectively. Hydromagnesite is more soluble than either magnesite or dolomite (Table 2), but was more likely to precipitate, at least initially, than the latter two minerals based on the model results. All other components in these waters slowly increased in concentration and other minerals did not precipitate until approximately 97% concentration. The resulting concentrated solution is dominated

by sodium, with alkalinity (HCO_3^- + CO_3^{2-}), sulfate (SO_4^{2-}), and chlorine. At 97% concentration, thenardite (Na_2SO_4) precipitated out of solution and at 99% concentration, thermonatrite (Na_2CO_3•H_2O) and halite (NaCl) precipitated out of solution. CHEMCHAU also predicted that hydromagnesite formed 30 times more precipitate than calcite formed; that is, the mass of hydromagnesite that precipitated from solution was 30 times greater than calcite. Additionally, CHEMCHAU predicted that halite formed 20 times more precipitate than hydromagnesite after 97% concentration; that is, the mass of halite that precipitated from solution was 20 times greater than hydromagnesite.

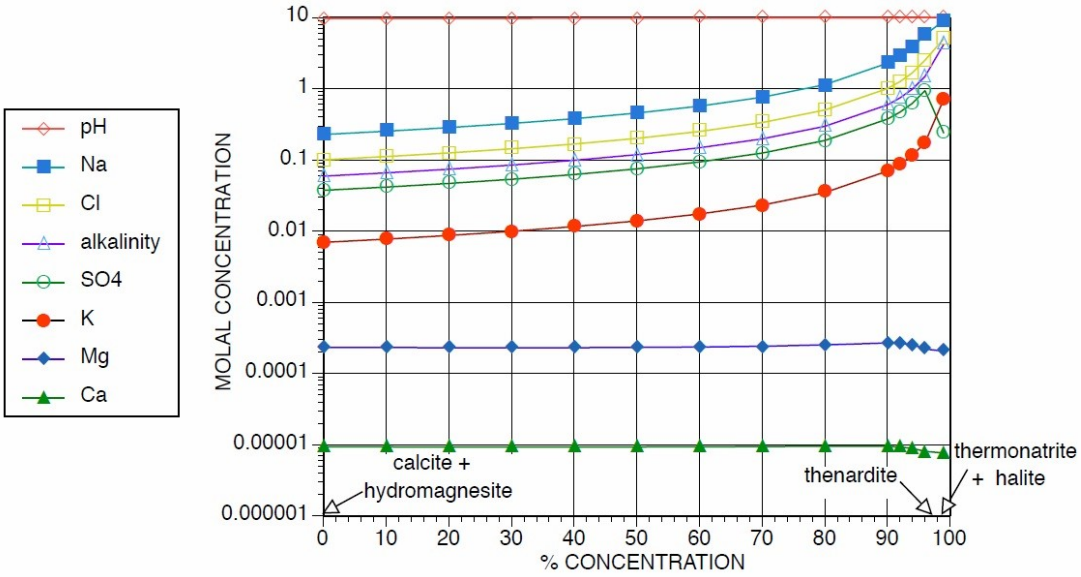

Figure 4: Walker Lake constituent concentration as the water was concentrated at 80° C using the CHEMCHAU model. Arrows point to precipitation of compounds: calcite ($CaCO_3$) and hydromagnesite [$Mg_5{\cdot}(CO_3)_4{\cdot}(OH)_2{\cdot}4H_2O$] precipitate initially and thenardite (Na_2SO_4), thermonatrite ($Na_2CO_3{\cdot}H_2O$), and halite (NaCl) precipitate after 97% concentration.

1.6.2 Experimental scaling of MD membranes

Even at higher concentration factors of feedwater (including at supersaturation), DCMD experiences minimal driving force reductions and salt

rejection can be nearly 100% [47]. However, the likelihood of scaling at the membrane surface increases as a result of high concentrations in the feed [53].

Additional scaling issues may arise due to the higher feed temperatures necessary for DCMD. Some constituents, including gypsum ($CaSO_4$) and calcite, exhibit inverse solubility with increasing temperature, magnifying precipitation and thus, scaling [54]. It has also been shown that the size of the crystals that form on the membrane surface increases with increasing feed temperature [55]. Higher temperatures also promote quicker scale formation and rapid flux decline [53]. It was shown that formation of scale decreased heat transfer in DCMD [46], reduced membrane hydrophobicity [55], and reduced vapor transfer [55], all of which will decrease the overall driving force, and thus flux, of the system.

Many MD investigations with waters containing calcite, a common precipitate of supersaturated surface waters, have been previously performed [54-57]. In a study of feedwater containing calcite in a DCMD system, distillate flux was constant despite the feed solution being constantly supersaturated with calcium [55]. In that case, calcite did not scale the membrane or cause flux decline. Another study focused on alkaline scale, which consists of calcite, brucite [$Mg(OH)_2$], and admixtures of both [53]. In this study, 37 °C was the minimum temperature required in the feed solution (tap water generated from a lake) to precipitate calcite. Alkaline scale was dependent on feed temperature, concentration of constituents in the feedwater, recirculation time over the membrane surface, and additional flow conditions (e.g., velocity). Finally, flux decline was observed in the system due to the formation of alkaline scale.

Co-precipitation of phosphate with calcite from surface waters was previously investigated [58]. Calcite was supersaturated in lake water and co-precipitated out with phosphorous. Another previous investigation showed that the nucleation and crystal growth rates of calcium solids, specifically calcite, that form on surfaces or precipitate from solutions are inhibited, or slowed, by the presence of magnesium ions [59]. The scale deposit that formed from waters containing both ions was proportional to the ratio of the ions (Mg^{2+}/Ca^{2+}) dissolved in the solution. Additionally, the presence of magnesium ions altered the crystal formation of calcite. Other forms of calcium carbonate, specifically vaterite ($CaCO_3$), were suppressed by the presence of magnesium, resulting in mainly calcite scalant. Additionally, the presence of dissolved sodium and sulfate species (i.e., thenardite) significantly reduced the precipitation of calcite, or increased the solubility of calcite, in seawater [60]. These effects of co-precipitation were seen in solutions containing high concentrations of magnesium, sodium, calcium, and carbonates. This co-precipitation phenomenon has caused unexpected precipitants, such as hydromagnesite instead of magnesite [57].

1.6.3 DCMD cleaning cycles

Membrane cleaning is necessary to remove scalant from the membrane surface and recover DCMD flux. Previous studies have utilized both basic and acidic solutions for membrane cleaning [10, 54]. A solution containing disodium ethylenediaminetetraacetic acid (Na_2EDTA) and sodium hydroxide (NaOH) has been shown to sufficiently recover flux from membranes used to treat brine solutions [10],

and a solution containing citric acid ($C_6H_8O_7$) was able to successfully remove calcite scale from membranes used to desalinate surface waters ($CaCO_3$ scale) [54]. Both EDTA and citric acid are strong chelating agents and can diminish divalent cation (e.g., Ca^{2+}) reactivity at the membrane surface [61]. Based on CHEMCHAU modeling, the most likely precipitates from Walker Lake water are hydromagnesite and calcite, both of which contain divalent cations (i.e., Ca^{2+} and Mg^{2+}).

1.7 Objectives

The overall objective of this investigation was to evaluate the effect of evaporation suppression and membrane scaling/cleaning on predicted and experimental freshwater production from a coupled SGSP/DCMD system. The subobjectives were to 1) determine the best cover/element for evaporation suppression with consideration of the desire to increase temperature and heat content in the solar pond; 2) predict precipitants that would likely form during concentration of Walker Lake water to fill the SGSP and during DCMD concentration; and 3) evaluate the ability to remove scalant and recover flux in DCMD.

2. Materials and Methods

2.1 Solar Pond

An SGSP that was constructed as described in Suarez et al. [1] was used to perform all experiments. The solar pond was constructed with three vertical walls and one diagonal wall at a 45 degree angle. The top water surface area was approximately 1.9 m^2, the bottom water surface area was 1.0 m^2, the water depth was approximately 1.0 m, and the overall water capacity was approximately 1.5 m^3. The angled wall formation resulted in a loss of available heat in the LCZ due to the lower solar pond volume when compared to a solar pond with four vertical walls. Overall, steady-state water production values were influenced by the small volume of the LCZ when compared to the surface area of the solar pond.

The solar pond was located in a laboratory setting so that there was consistent daily sunlight over the solar pond surface, no disturbances from weather (e.g., wind, rain, or clouds), and no large daily temperature fluctuations. In order to mimic the sunlight spectrum, three high-intensity discharge lamps were positioned over the surface of the solar pond (Figure 5). The three lamps were each powered by a Super Grow 1000 W halide/sodium convertible ballast (Hydrofarm Inc., Petaluma, CA) that each lit an EYE Hortilux Super Blue (Mentor, OH) dual arc bulb. These lamps covered a spectrum of approximately 350 to 900 nm, which includes the ultraviolet, visible, and near-infrared wavelengths. High water turbidity and salt concentration can cause decreasing intensity of light penetration with increasing depth due to an increase in the reflection of photons inside the water column [39, 40, 62]. To obtain a general idea of the effects that turbidity and increased salt concentration have on the

depth of light penetration, photon measurements were taken at different depths inside the solar pond (Figure 6). Measurements were made using an Ocean Optics spectrometer (Dunedin, Florida), which was lowered into the solar pond vertically after the solar pond was filled with salt water.

Figure 5: Salinity gradient solar pond with three high-intensity discharge lamps, each consisting of a halide/sodium bulb in order to replicate natural sunlight. Each bulb is powered by a ballast.

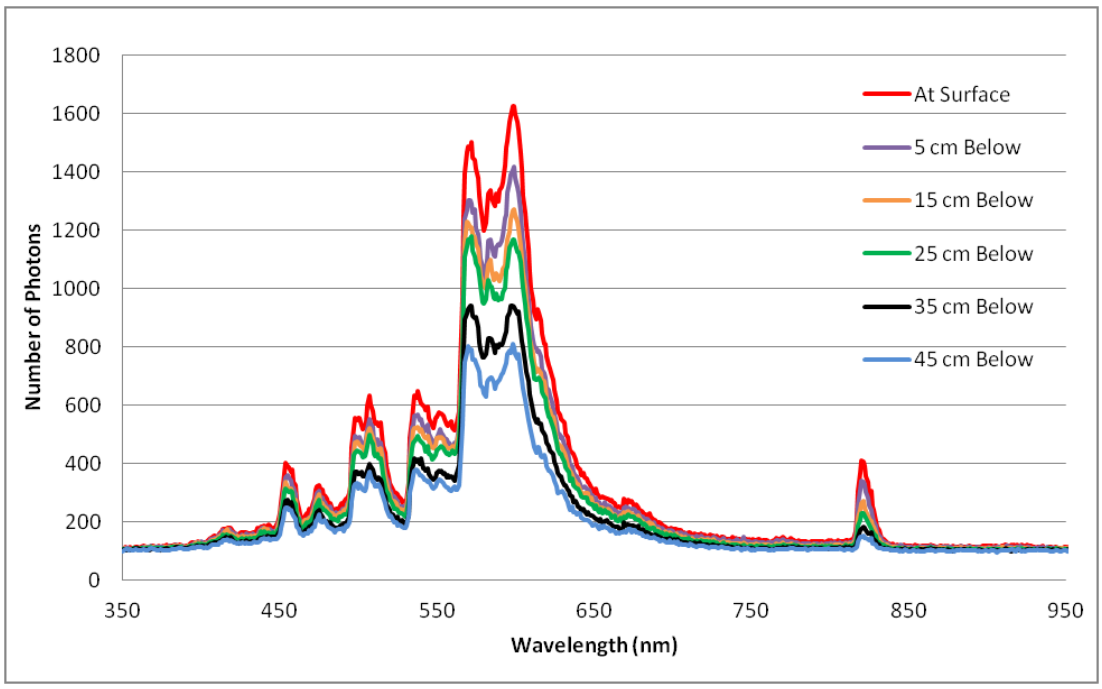

Figure 6: Lamp discharge intensity with increasing depth of the solar pond.

It can be seen that photon count decreases with increasing depth. At 45 cm below the surface, photon intensity is generally half the value of photon intensity measured at the solar pond surface over the measured spectrum. Most solar ponds have more than 45 cm of depth above the LCZ and are thus susceptible to reduced photon penetration to the LCZ. Additionally, the highest penetration of light into the pond occurs in the visible region (Figure 6). Wavelengths in the ultraviolet and near-infrared regions are unable to penetrate deeply into the water column; this lack of penetration agrees with a previous study [63].

A shielded HPMC45-L sensor (Campbell Sci., Logan, UT) measured air temperature and relative humidity at the water surface. A Q-7.1 net radiometer (Campbell Sci., Logan, UT) was positioned approximately 10 cm above the water surface and was used to measure net radiation. Two LP02 pyranometers (Hukseflux, Delft, The Netherlands) were also positioned 10 cm above the water surface to

measure shortwave radiation; one measured the direct radiation emitted from the lamps and the other measured the reflected radiation off the solar pond. All air temperature and radiation data were collected using a CR23X datalogger (Campbell Sci., Logan, UT), which was set to record at 5-min intervals. Electrical conductivity of the salt water in the solar pond was measured using epoxy SK23T electrodes (Van London-pHoenix Company, Houston, TX) at 10 cm depth intervals. A modular D230 multi-channel datalogger (Consort, Turnhout, Belgium) recorded the electrical conductivity data at 5-min intervals. One vertical wall of the solar pond also contained ten manual sampling ports, which enabled manual removal of water from every 10 cm of depth. Water density was monitored using a DA-110 M portable density meter (Mettler Toledo, Columbus, OH) on weekly samples withdrawn from the sampling ports.

A vertical high-resolution distributed temperature sensing (DTS) system provided a continuous, highly accurate temperature profile throughout the depth of the solar pond [64]. In this system, a laser signal is sent down a length of fiber optic cable and the strength of the backscattered light that is returned to the DTS corresponds to the temperature at a certain distance along the cable. Approximately 200 m of fiber optic cable was coiled around a 1.5 in. diameter PVC pipe and was covered with heat shrink to protect the cable from salt exposure. This 'DTS pole' was secured inside the solar pond vertically and the fiber optic cable was connected to a Sensornet Sentinel computer system (Sensornet Sentinel Instrument, Sensornet Ltd., Herthfordshire, England). The fiber optic cable ran from the DTS computer system, through two water baths that were kept at constant temperatures of 20 and 50 °C for

calibration purposes, and then into the solar pond (around the DTS pole). The Sensornet read temperatures at every 2 m of cable; considering that the cable was coiled around a pole, temperature readings were taken from every 1.1 cm of depth inside the solar pond.

2.1.1 Solar pond filling and initial temperature evolution

The solar pond was first filled with salt water on January 1st, 2011. The salinity gradient that was artificially created in the solar pond is shown in Figure 7. The solar pond was first filled with 24.5% by weight sodium chloride (NaCl) solution until a height of 60 cm was reached inside the solar pond; this was the depth of the LCZ. After this, 5 cm layers of decreasing salinity solutions were added until a solar pond height of 100 cm was reached; this comprised the NCZ. These layers were added by slowly pumping a pre-mixed solution into the solar pond. The salt solution was pumped onto a floating plastic disc with holes throughout the bottom that allowed the pumped solution to slowly drain on top of the previous layer in the solar pond. Density was consistently monitored via manual sampling throughout the filling process to ensure that mixing did not occur between the added layers. Finally, 5 cm of freshwater was added to the top of the solar pond; this was considered to be the UCZ. These three zones brought the total depth inside the solar pond to 105 cm. At this time, the temperature profile in the solar pond was expected to be nearly uniform and near room temperature.

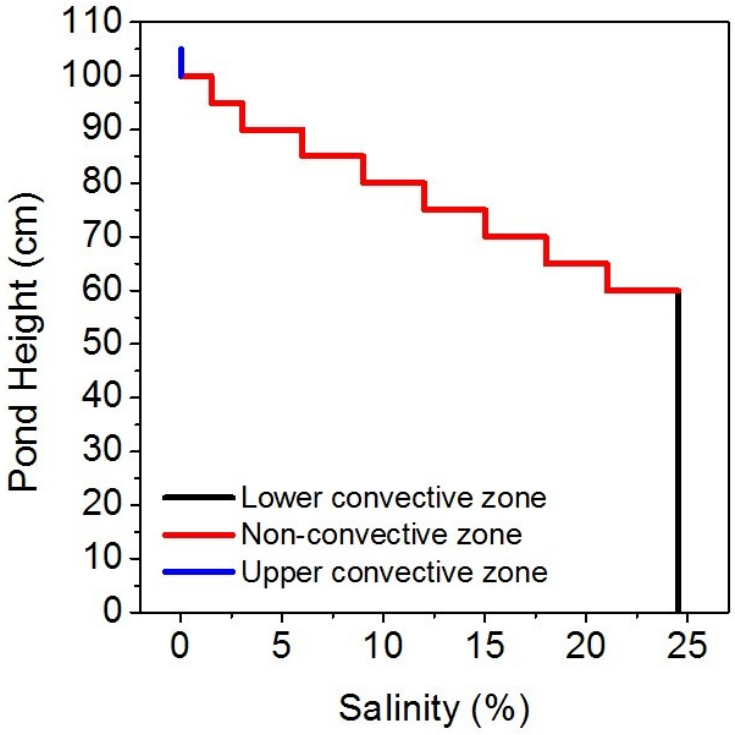

Figure 7: Solar pond salinity. The LCZ consisted of 24.5% NaCl and occupied the bottom 60 cm, the NCZ consisted of decreasing NaCl concentration and occupied the solar pond from 60 cm to 100 cm, and the UCZ consisted of freshwater and occupied the top 5 cm.

A black pond liner was placed over the solar pond for 5 days to prevent any radiation penetration [33] and to give the pond layers in the NCZ time to settle (no density changes as a result of temperature changes). On January 6th, the pond liner was then removed to allow the solar pond to reach quasi steady-state before experiments commenced. The thermal evolution of the uncovered solar pond with 12-hour light/12-hour dark cycles is shown in Figure 8. On January 6th, the lights were turned on from 06:00 to 18:00. Operating the lights in 12-hour light/12-hour dark cycles resulted in two thermal steady-states; one occurring during each light period and one occurring during each dark period. The three thermal zones in the solar pond (UCZ, NCZ, and LCZ) can clearly be seen in the February 5th temperature profile; the UCZ was from 0 to 5 cm depth, the NCZ was from approximately 5 cm to

approximately 55 cm depth, and the LCZ was from approximately 55 cm to approximately 100 cm depth. The first thermal quasi steady-state, defined as being when little variation occurred daily in the overall temperature of the solar pond for both the 12-hour light/12-hour dark daily cycles, was reached in the solar pond on February 5th.

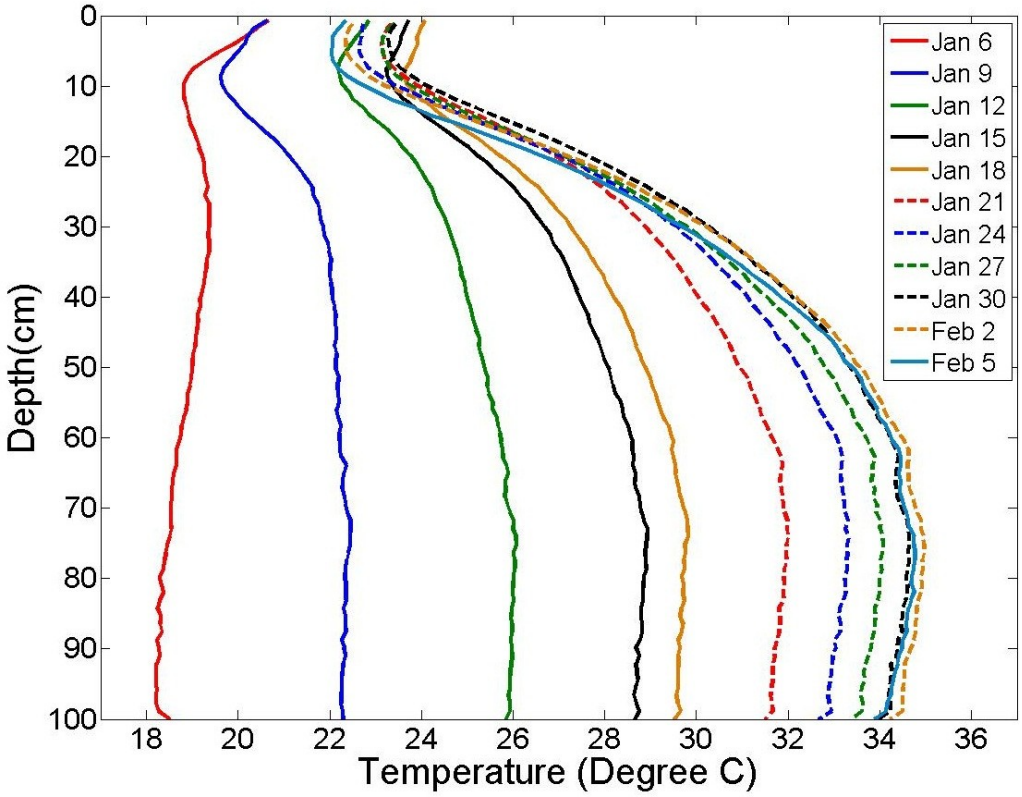

Figure 8: Heat content evolution of the uncovered salt gradient solar pond. Lights were operated beginning on January 6th in 12-hour light/12-hour dark cycles.

The thermal evolution of the solar pond at the surface and at depths of 50, 60, and 92 cm is shown in Figure 9. The 12-hour light/12-hour dark cycles of the overhead lamps can be seen in the diurnal temperature profiles with respect to time (days). The peaks and valleys of each line represent the end of the light cycle and the end of the dark cycle, respectively. During initial solar pond operation, the surface of the solar pond reached its maximum temperature in approximately 10 days, and had

higher daily fluctuations. The lower three depths reached their respective maximum temperatures after approximately 26 days, and had lower daily fluctuations than those observed at the surface surface.

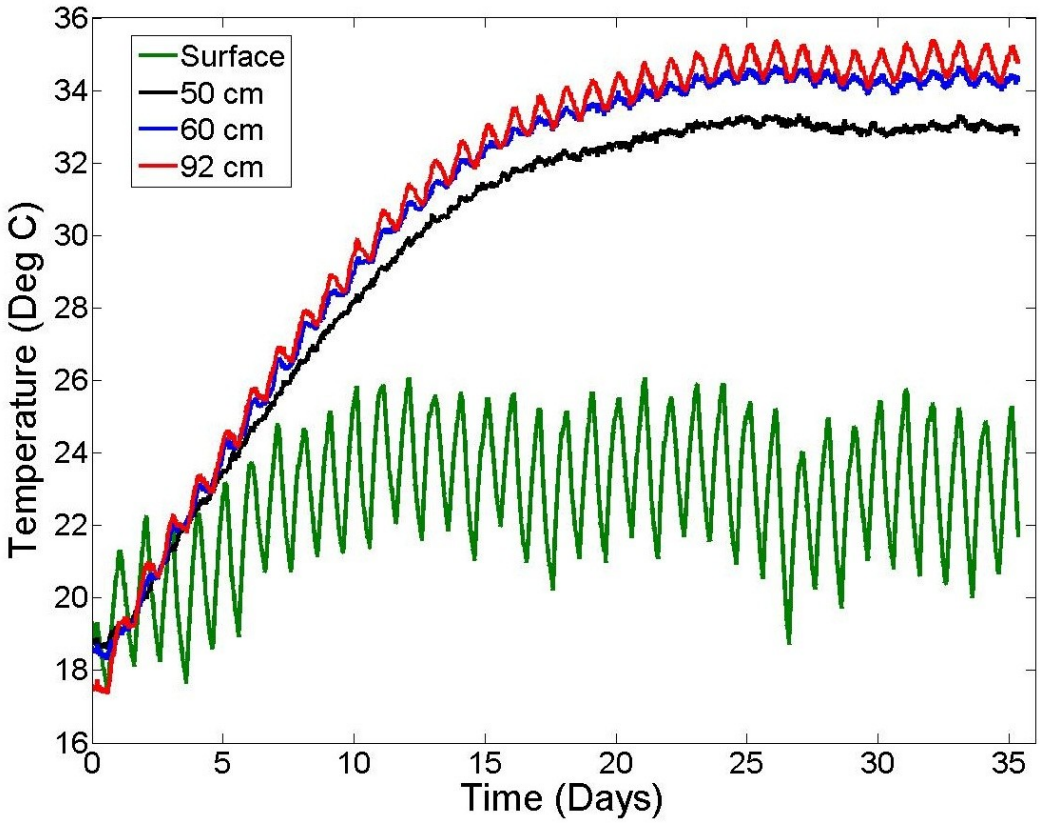

Figure 9: Thermal evolution of an uncovered solar pond at the surface and three depths of 50, 60, and 92 cm.

2.2 Evaporation reduction experiments and temperature evolution of the solar pond covered with the covers/elements

Three different covers/elements were tested on the solar pond surface: a continuous plastic cover, non-treated polystyrene petri dishes, and polyethylene terephtalate glycol (PETG) half spheres. Petri dishes were readily available for use in the laboratory and the dishes were fully transparent, so light blockage from shortwave

radiation would be minimized. The half spheres were chosen because of their transparency and buoyancy [65], two important criteria for evaporation suppressing covers/elements. Both of the floating elements chosen had emissivity values similar to water [66]. The evaporation suppression of each cover/element was tested over the time period that it took to achieve thermal quasi steady-state. Solar pond temperatures were confirmed by observing the overall temperature gradient with the DTS.

After selection of the best cover/element, heat was extracted from the LCZ by recirculation of the LCZ solution through an external heat exchanger. The other stream coupled to the heat exchanger was freshwater. After passing through the heat exchanger, the freshwater entered the DCMD membrane module; distillate recirculated on the opposite side of the membrane. Both the feed and distillate temperatures at the inlets and outlets of the membrane module were monitored using four PRTF-10 RTD probes (Omega, Stamford, CT) coupled to an NI 9217 4-Channel analog module (National Instruments, Austin, TX). Two variable-flow console drives were located before the membrane module on the feed and distillate loops. Excess distillate volume was measured using an external Mettler Toledo scale (Columbus, OH).

After the completion of the SGSP/DCMD experiment, the lights were allowed to remain on for 24-hours per day. In this way, the solar pond reached one thermal steady-state with a maximum temperature in the LCZ. When this new steady-state was achieved, the LCZ solution was once again recirculated to remove heat. In this way, a maximum water production rate for the laboratory system (with constant light operation) was determined.

2.2.1 Transmittance of covers

The transmissivities of the three covers/elements were measured using two methods. In the first method, radiation penetration through each cover/element was measured using a Cary 300 Bio UV-Visible spectrophotometer (Agilent Technologies, Santa Clara, CA). Samples of each cover/element (5 cm x 1 cm) were prepared and placed in the cell holder of the spectrophotometer with the flat surface perpendicular to the instrument's optics sensor. In addition to the three covers/elements, blanks and deionized water samples were also measured with the spectrophotometer.

The petri dishes allowed the highest radiation penetration for the recorded spectrum (Figure 10). The half spheres generally allowed 10-15% less radiation than the petri dishes, and the continuous plastic cover allowed significantly less radiation penetration than the two element types. Additionally, all covers/elements have less transmissivity for shorter wavelengths (ultraviolet) and more transmissivity for longer wavelengths (visible and near-infrared). The elements allow penetration of shortwave radiation (ultraviolet, visible, and near-infrared) comparable to the water sample. Most of the energy transmitted by the sun is in the form of shortwave radiation. Therefore, the higher penetration of these wavelengths can lead to higher temperatures throughout the solar pond [63]. Shorter wavelengths (ultraviolet and visible) are able to penetrate deeper into a water column when compared to longer wavelengths (NIR and longer). This allows the LCZ to collect more radiation, and, as a result, a higher temperature in the LCZ can be reached.

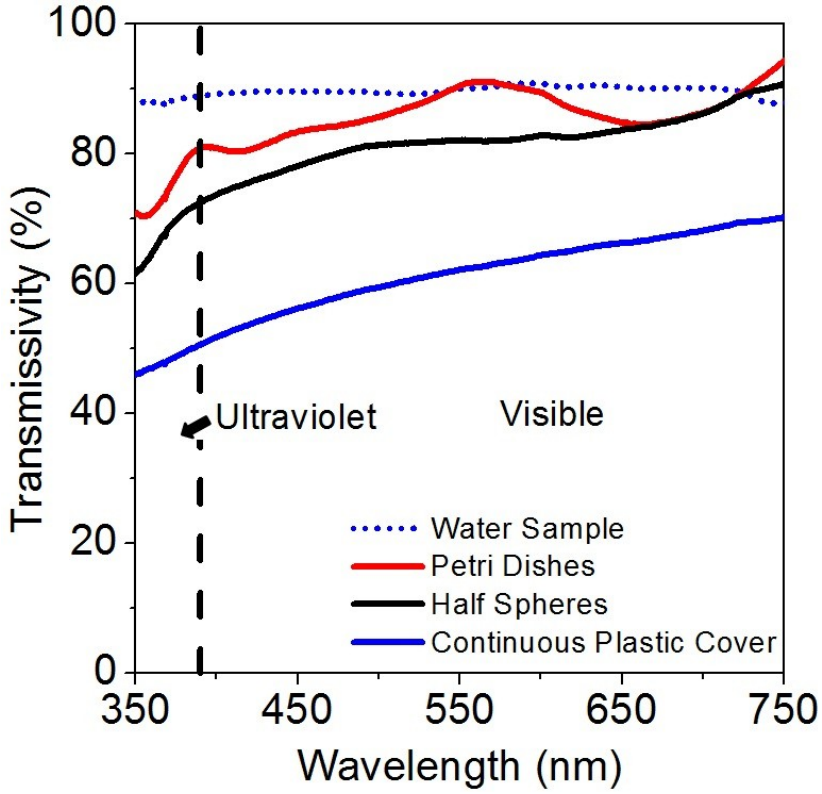

Figure 10: Transmissivity over the visible spectrum for a water sample, the petri dishes, the half spheres, and the continuous plastic cover as a function of wavelength.

In the second method, a MQ-200 (Apogee, Logan UT) light sensor measured the tranmissivities of the three covers/elements in natural sunlight. Results using the quantum meter are shown in Table 3. The meter approximates the total quantity of photons, or quantums, radiated by the sun between 400 and 700 nanometers. Placing the meter under each cover/element under direct sunlight provides a general idea of how transparent each cover/element is. As seen in Table 3, and in agreement with the spectrometer data, the petri dishes allow the highest amount of photons to pass through the cover, the half spheres allow the second highest amount of photons, and the continuous plastic cover allows the least amount of photons to pass through. However, the difference in photon transmission through the petri dishes and half spheres, and between the half spheres and continuous plastic cover are both less than

10%. Experimental temperature data from the solar pond was used to confirm that the petri dishes were best for radiation penetration.

Table 3: Natural sunlight radiation penetration through each of the three covers/elements.

Cover Type	Quantums
No Cover	1360
Petri Dishes	1280
Half Spheres	1233
Continuous Plastic Cover	1155

2.2.2 Selected covers/elements and percent coverage of the solar pond

First, the solar pond was brought to thermal quasi steady-state with the surface of the solar pond open to the environment without covers/elements. The operation of the solar pond without covers/elements was used to determine the baseline evaporation rate and the temperature gradient present prior to heating.

The solar pond was then fully covered with a continuous plastic cover. The 12 Mil Clear Solar Pool Cover (Leisure Living, Tonawanda, NY) was cut to fit over the entire solar pond surface with 10 cm of extra length on each side to attach to the four walls directly above the water surface (Figure 11). This overlap of the solar pond walls eliminated almost all water-air contact on the surface of the solar pond and prevented the continuous plastic cover from moving around on the surface. Approximately 99% coverage was possible with the continuous plastic cover due to water-air contact around the DTS pole and at the UCZ recirculation pipes.

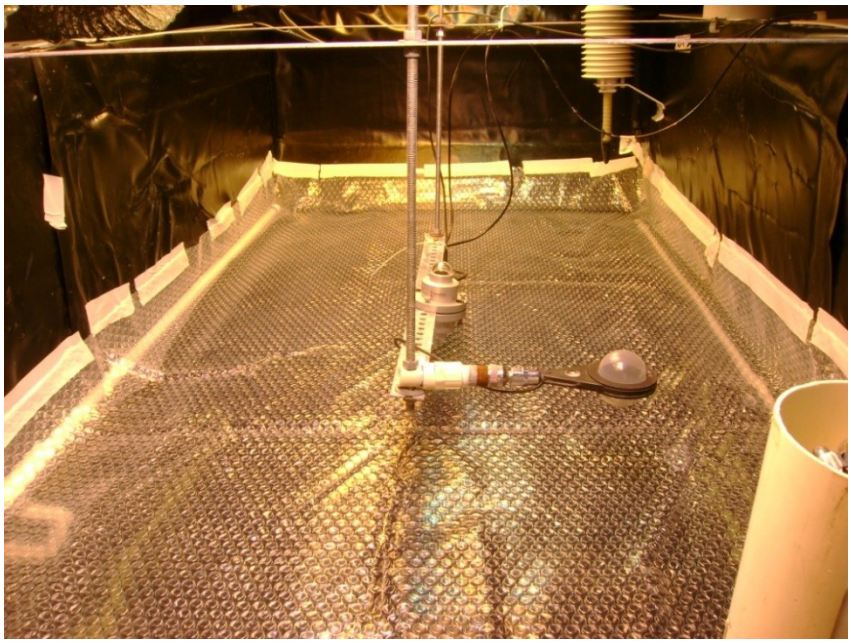

Figure 11: Salinity gradient solar pond with continuous plastic cover installed.

After thermal quasi steady-state was achieved with 99% coverage of the continuous plastic cover, equal-sized openings were cut into the cover to achieve solar pond percent coverages of 95, 90, 85, 80, 75, 70, and 60% (Figure 12). For 95% coverage, 21 squares (2 cm x 2 cm) were cut into the cover; to achieve lower solar pond coverages, the size of each square was increased incrementally. The solar pond was allowed to reach a new thermal quasi steady-state at each of the percent coverages.

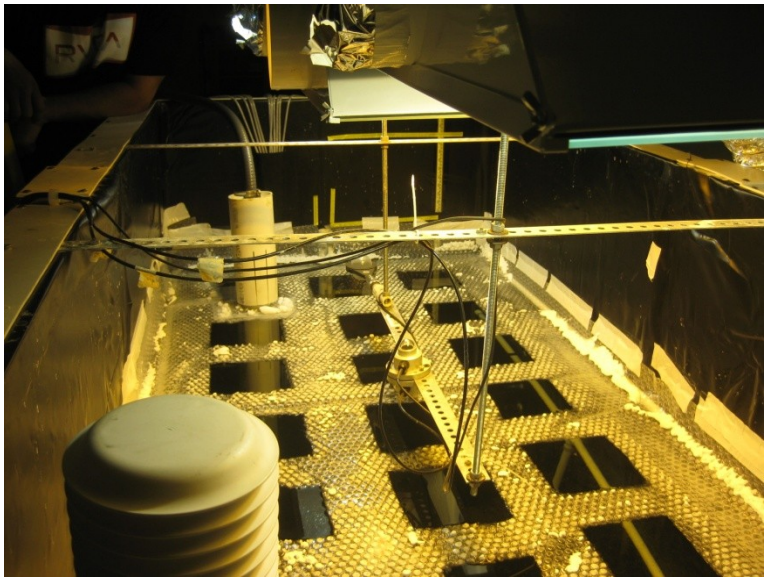

Figure 12: Salinity gradient solar pond at 60% coverage with the continuous plastic cover.

After completion of the continuous plastic cover experiments, the solar pond was uncovered and allowed to reach a thermal quasi steady-state once again. Following this, the tops of 96 bacteriological non-treated polystyrene petri dishes (150 mm x 15 mm; BD Falcon, Sparks, MD) were placed on the surface of the solar pond. The petri dish tops were placed with the open side upwards (Figure 13). When the petri dishes were tested with the open side placed downwards, they were unstable on the water surface and resulted in some petri dishes becoming unstable and sinking below the surface. The maximum area of coverage for this transparent floating element was approximately 88%. This maximum coverage was calculated by multiplying the number of petri dishes covering the solar pond by the individual petri dish surface area and then dividing by the measured solar pond surface area. Solar pond percent coverage was incrementally decreased from approximately 88 to approximately 80, 85, 70, 60, 50, 40, 30, and 10% by sequentially removing a calculated number of elements from the solar pond surface.

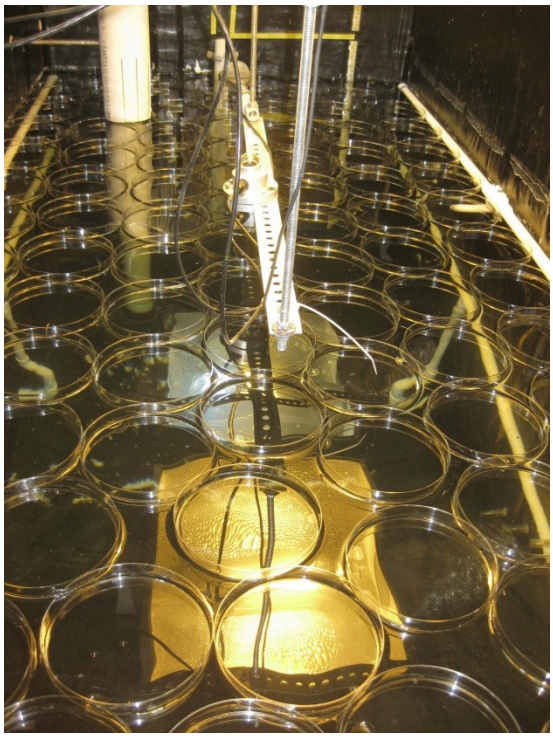

Figure 13: Fully covered solar pond with petri dishes.

After completion of the petri dish experiments, the solar pond was uncovered and allowed to reach a thermal quasi steady-state once again. Following this, fully transparent PETG 60-gauge half spheres (Barnard LTD, Chicago IL) were placed on the solar pond surface with their convex dome facing up. These experiments started with approximately 10% coverage (Figure 14). Whereas the bottom of each petri dish had direct contact with the water surface, the half spheres contained trapped air between the water surface and the concave dome. Additional half spheres were added incrementally until the maximum percent coverage (approximately 97%) was achieved with 77 half spheres. Similar to the petri dish calculation, percent coverage was calculated by multiplying the number of half spheres covering the solar pond by the individual half sphere bottom surface area and then dividing by the measured solar pond surface area. However, due to the half spheres rocking, or tilting, on the

water surface, there was some overlap that occurred along the edges of the half spheres. This instability of the half spheres resulted in higher percent coverage estimations than were actually achieved. Since this overlap was unable to be quantified, percent coverage was estimated using the petri dishes method.

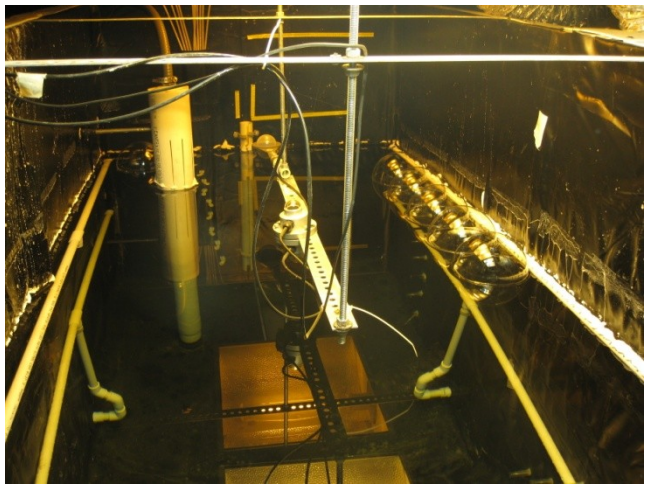

Figure 14: Solar pond with seven half spheres, resulting in approximately 10% coverage.

2.2.3 Experimental evaporation measurements

An external FG-200KAL scale (A&D Engineering, Inc., San Jose, CA) was used to constantly monitor evaporation rates by weighing a 60-L water tank used to replenish water evaporated from the solar pond surface and recording this weight every two minutes. A variable-flow console drive (Cole-Parmer Console drive, Vernon Hills, IL) recirculated freshwater from this tank into the UCZ of the solar pond. An inlet pipe installed at a vertical height of 102 cm on the west wall supplied freshwater into the UCZ at a constant flow. Water was allowed to drain by gravity from an outlet pipe installed at a vertical height of 105 cm on the east wall. The outlet pipe returned the water from the UCZ to the freshwater tank. This enabled a constant water depth of 105 cm to be maintained in the solar pond at all times. As water

evaporated from the solar pond surface and the solar pond depth was kept constant at 105 cm, the water loss due to evaporation was seen in the freshwater tank, which slowly drained over time. This tank was refilled every few days with tap water as necessary.

2.3 Coupled SGSP/DCMD system and DCMD performance model

Because previous coupled SGSP/DCMD system modeling indicated that evaporative losses from the solar pond surface were on the same order of magnitude as freshwater production [1], evaporation suppression is necessary to have a positive water budget. Additionally, any increased heat that results from evaporation suppression likely will contribute to more available heat in the LCZ and increased freshwater flux. Flux experiments were performed on the closed-loop bench-scale membrane test system shown in Figure 15. The feed tank contained heated deionized water circulating through a heat exchanger paired with circulating LCZ solution. The distillate tank contained two liters of deionized water cooled to the distillate temperature (20 °C). Both the feed and distillate temperatures at the inlets and outlets of the membrane module were monitored using four PRTF-10 RTD probes (Omega, Stamford, CT) coupled to an NI 9217 4-Channel analog module (National Instruments, Austin, TX). Two variable-flow console drives were located before the membrane module on the feed and distillate loops and recirculated both streams at a constant flowrate of 1.5 L/min. Acrylic flowmeters (FR4000, Key Instruments, Trevose, PA) monitored the feed and distillate flow rates. Excess distillate volume was monitored using an external Mettler Toledo (Columbus, OH) scale.

Temperatures, pressures, and overflow distillate weight readings were taken every two minutes during system operation.

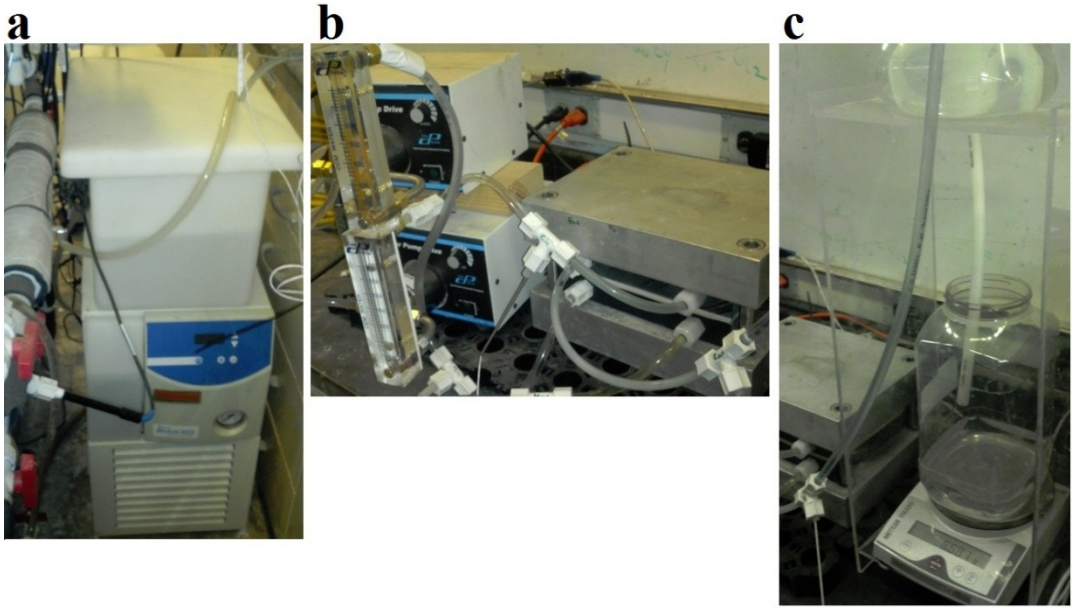

Figure 15: DCMD system for flux experiments, including a) heat exchanger, feed tank, and chiller, b) feed and distillate pumps and membrane module, and c) scale and permeate overflow tank.

After the best cover was chosen based on evaporation suppression, solar pond temperature, and overall solar pond heat content, the solar pond was again covered with that cover and the coupled DCMD system was operated for 24 hours. Flux was measured by weighing the excess distillate every two minutes. From this, a steady-state flux for 24-hour operation was achieved. In this way, we can compare results to Suarez et al. [33].

2.3.1 DCMD performance model

A previously developed DCMD model [1] was used to predict the DCMD flux that could be achieved using the heat collected in the solar pond LCZ. Feed and

distillate temperatures, flow rates, pressures, and freshwater flux were determined from operation of the coupled SGSP/DCMD system. Membrane characteristics were also input into the model. These included membrane thickness, average pore size, tortuosity, and porosity [67]. DCMD model predictions were compared with experimental results. The freshwater flux from the DCMD system was determined using the following equation [68]:

$$J = C_m * (P_{f,m} - P_{p,m}) \quad (1)$$

where J is freshwater flux (m^3 per day-m^2 of membrane area), C_m is the distillation coefficient (m^3 per m^2-day-Pa), and $P_{f,m}$ and $P_{p,m}$ are the vapor pressures (Pa) at the feed and permeate surfaces of the membrane, respectively. The distillation coefficient (C_m) is a function of membrane pore size, thickness, porosity, tortuosity, and the properties of the bulk fluid [69]. Membrane characteristics used in the model are shown in Table 4.

Table 4: Membrane characteristics used in the DCMD model.

Property	Value
Porosity (%)	80.1 ± 18
Tortuosity	1.79 ± 0.55
Membrane Thickness (μm)	67 ± 17
Average Pore Size (μm)	0.1

Vapor pressure at the membrane surface was estimated using the Antoine equation [70]:

$$\text{Log } P = A - \frac{B}{C+T} \quad (2)$$

where P is the vapor pressure (mmHg), A, B, and C are component-specific constants, and T is the temperature at the membrane surface, which can be calculated

from known membrane module properties [1, 71, 72]. Average bulk feed and permeate temperatures were estimated based on the temperatures into and out of the membrane module. Average bulk feed temperature was calculated by:

$$T_{f,b} = \frac{T_{f,b,in} + T_{f,b,out}}{2} \quad (3)$$

The feed temperature at the membrane surface was calculated by:

$$T_{f,m} = T_{f,b} - \frac{\frac{T_{f,b} - T_{p,b}}{h_f}}{\frac{1}{h_f} + \frac{1}{h_p} + \frac{1}{h_c + h_v}} \quad (4)$$

and the permeate temperature at the membrane surface was calculated by:

$$T_{p,m} = T_{p,b} + \frac{\frac{T_{f,b} - T_{p,b}}{h_p}}{\frac{1}{h_f} + \frac{1}{h_p} + \frac{1}{h_c + h_v}} \quad (5)$$

where $T_{f,b}$ is the temperature of the bulk feed solution, $T_{p,b}$ is the temperature of the bulk permeate solution, h_f is the heat transfer coefficient of the feed (W per m^2-K), h_p is the heat transfer coefficient of the permeate, h_c is the heat transfer coefficient for conduction across the membrane (a function of the thermal conductivities of the membrane, membrane thickness and porosity, and the air trapped inside the membrane pores), and h_v is the heat transfer coefficient for vapor flow through the membrane.

2.4 Walker Lake concentration analyses and bench-scale DCMD concentration experiments

2.4.1 Walker Lake water collection

Walker Lake water was used as feedwater for DCMD scaling experiments. Samples were taken from the end of the boat dock at the Sportsman's Beach boat

access ramp located on the western shore of Walker Lake, near Hawthorne, NV (Figure 16). Before water samples were taken, a visual inspection of the Walker Lake collection site was performed; this included observation of any potential pollution or contamination sources and the condition of the water (e.g., clarity, cloudiness, color, odor, foaminess). Water temperature data was taken.

Figure 16: Collection site at Sportsman's Beach, Walker Lake, Hawthorne, NV.

Samples were taken in 20 L polyethylene resin collapsible liquid shipping containers (McMaster-Carr, Santa Fe Springs, CA). Prior to filling, each container was rinsed with Walker Lake water twice and then each container was filled with a full 20 L; that is each container was filled until essentially no head room remained. The containers were sealed and transported to the University of Nevada Environmental Engineering laboratories were they were stored at a constant 5 °C until used for DCMD testing.

2.4.2 Aquatic chemistry analyses (CHEMCHAU [52] and OLI Analyzer Studio 3.2)

An aquatic chemistry analysis was performed using OLI Analyzer Studio 3.2 (OLI Systems Inc., Morris Plains, NJ). Analyzer Studio 3.2 is an equilibrium chemical thermodynamics model [73, 74] that predicts possible precipitants from a fixed water analysis. The aqueous thermodynamic model [73] used was based on published data and utilized the Helgeson equation of state [75] for polynomial fits. The thermodynamic framework can run over a larger temperature range than CHEMCHAU. Additionally, there are two available databanks, public and geothermal, that contain similar solid speciation as CHEMCHAU. The public database contains most thermodynamic data necessary for surface water calculations. The geothermal databank was included in calculations in order to include additional Ca^{2+} and Mg^{2+} solid phases, such as hydromagnesite [73]. Walker Lake water data were entered into the model and an isothermal composition survey was conducted from 0 to 99.7% concentration. OLI Analyzer Studio 3.2 results were compared with the CHEMCHAU results described in Section 1.6.1.

2.4.3 Bench-scale experiments

Experiments were performed on the closed-loop bench-scale membrane test system shown in Figure 17. The feedwater tank for the scaling experiments held 18 L of Walker Lake water and the DCMD system was operated until 1.5 L of lake water remained in the feed tank, resulting in a 92% concentration of the feed volume. When this level of concentration was reached in the feed tank, the membrane was removed from the system and allowed to dry in an evaporative chamber. SEM imaging and

EDS analyses were performed on the dried membrane samples and XRD analysis was performed on the removed scale.

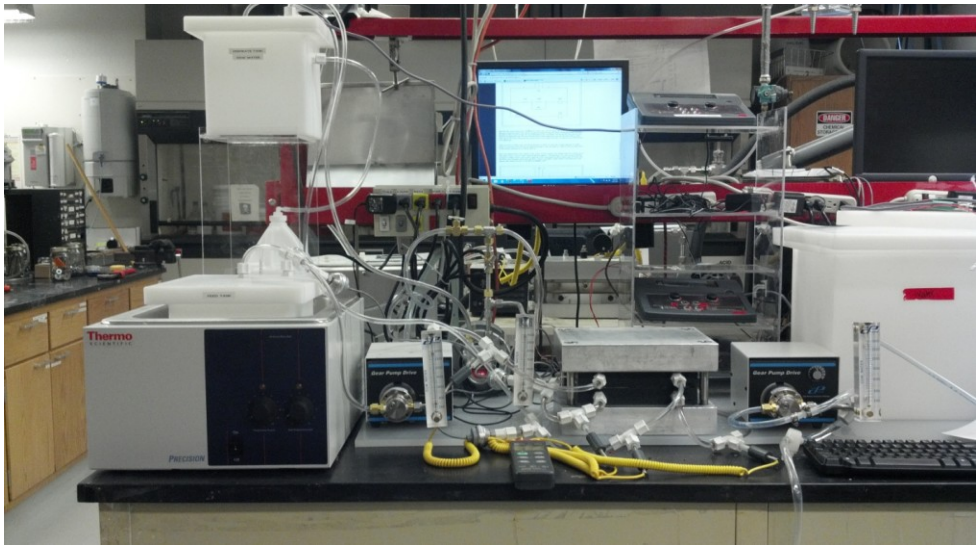

Figure 17: Bench-scale direct contact membrane distillation (DCMD) system.

2.4.4 DCMD cleaning cycles

Cleaning cycles were conducted when the DCMD system flux fell below 10% of the original flux during concentration of Walker Lake water. When this flux decline occurred, the system was stopped and a chemical cleaning cycle commenced. First, 4 L of deionized water were flushed across the membrane surface. Next, 2 L of cleaning solution was recirculated on the feed side for 30 min at ambient temperature (approximately 22°C). Two different types of cleaning solutions were tested: an acidic chemical cleaning solution that consisted of 0.240 M citric acid ($C_6H_8O_7$) and a basic chemical cleaning solution that consisted of 0.029 M Na_2EDTA and 0.058 M NaOH. Following the recirculation of one type of cleaning solution, 8 L of deionized water were flushed across the membrane to ensure all chemical solution was flushed from the system. Finally, the remaining feed solution of Walker Lake water was reintroduced to the chemically cleaned membrane. Additionally, two more cleaning

experiments were conducted with new membrane samples. After flux decline was observed, one membrane sample was cleaned with $Na_2EDTA/NaOH$, and the other was cleaned with citric acid. In concentrating the feed solution to 92% (8% of the initial volume), two cleaning cycles with citric acid solution were necessary.

2.4.5 Scanning electron microscope imaging and energy dispersive spectrometry analyses

Virgin, fouled, and chemically cleaned membrane samples were cut from the flat sheet membranes and attached to SEM slides using double-sided tape. Because SEM imaging required less than 1 cm^2 of membrane area per sample, numerous samples were able to be taken from each flat sheet membrane sample. The SEM slides were then Peltier-cooled, coated with platinum, and viewed under the SEM. Images of each SEM slide were taken at three magnifications: 500x, 5000x, and 10,000x. EDS analyses were performed on each SEM slide and provided the atomic percentage of all elements present on the sample surface, giving the elemental composition of any scale present on the membrane surface.

2.4.6 X-ray diffraction analysis

An XRD analysis was performed using a PANalytical X'Pert Pro (PANalytical, Almelo, Netherlands) in order to determine the crystal structure of the scale manually removed from the scaled membrane surface. The crystal structure of the powder was determined by focusing X-ray beams through the removed sample [76]. Both the transmitted beam through the sample and the diffracted beam were measured and compared to determine the structure. The average spacing between

atoms, the orientation of crystals, and the size and shape of the crystals were all recorded and used to determine the crystal structure, and therefore, the molecular formula, of the scale. Testing results were compared with known compounds in order to identify the scale composition.

3. Results and Discussion

3.1 Effects of percent coverage on solar pond evaporation

The measured evaporation rates during the course of daily operation for no cover/elements and for 95% coverage with the continuous plastic cover are shown in Figure 18. Evaporative losses decrease approximately 50% when the solar pond is 95% covered. The large peaks that occur at approximately 06:00 and sudden decreases that occur at approximately 18:00 correspond to the beginning and ending of the 12-hour light cycle, which occur at 06:00 and 18:00, respectively. These peaks and valleys are most likely caused by the sudden change in absolute humidity of the air above the water surface. When the lights above the solar pond turn on or off, the air temperature above the surface increases or decreases, respectively. As a result, the absolute humidity changes and affects the amount of evaporated water that can be held in the air [77].

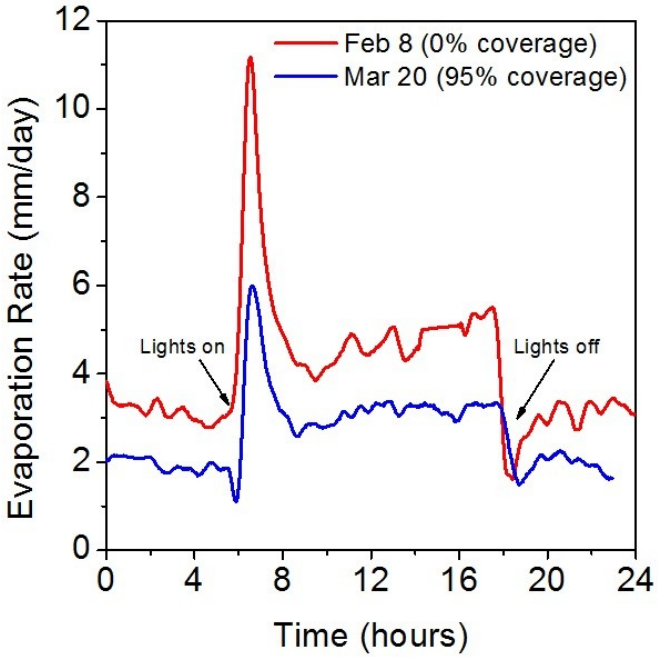

Figure 18: Evaporation from the solar pond surface during daily operation. The red line corresponds to no solar pond coverage, while the blue line corresponds to 95% coverage with the continuous floating cover.

The average measured daily evaporative loss that occurs from the solar pond surface for each of the three covers/elements as a function of percent coverage is shown in Figure 19. For all three covers/elements, daily evaporative loss increases as percent coverage of the solar pond decreases. Also, for all cases, evaporative loss generally follows a linear trend, which was also reported in a previous study [78]. An exception to the linear trend occurs for the continuous plastic cover above 95%, where the evaporation rate decreases sharply. As the first openings are made in the continuous plastic cover, water collects onto the surface of the cover along the edges of the openings due to the thickness of the cover. The increased air-water contact enhances evaporative losses. Similar results were seen in a previous study [79]. Additionally, the water that collects on the surface of the continuous plastic cover increases in temperature, further increasing evaporative losses. In comparison, water

did not collect onto the surface of the petri dishes and half spheres. Thus, the higher evaporative losses which occurred for the continuous plastic cover when compared to the petri dishes and half spheres at all coverages less than 99% are likely because of the ability of the water to pool more easily on the thin continuous plastic cover.

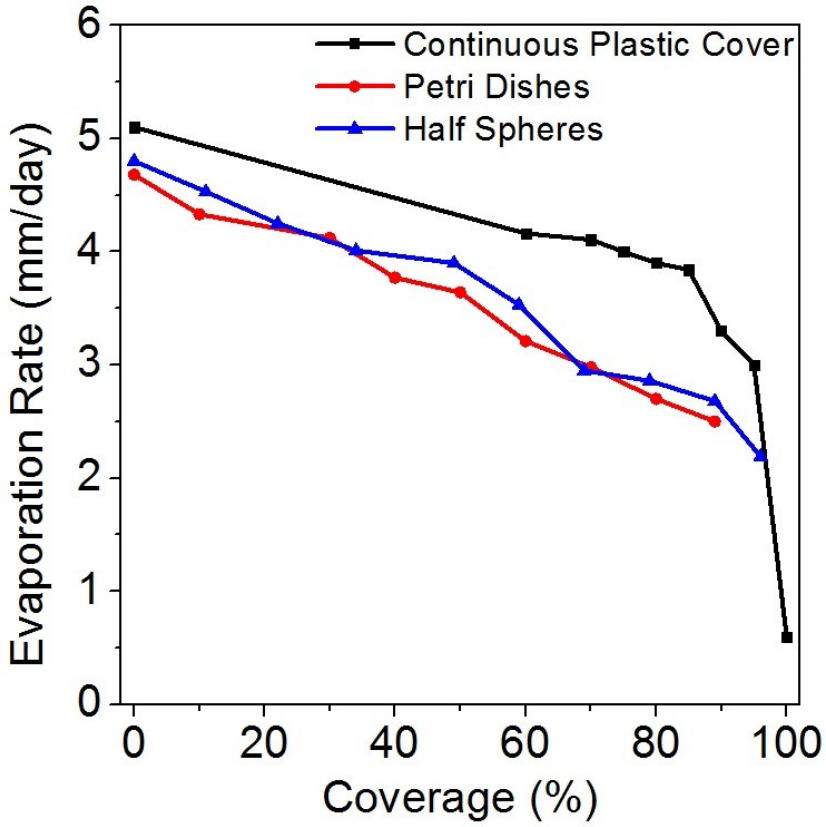

Figure 19: Evaporative losses from the solar pond surface as a function of percent coverage using the continuous plastic cover, petri dishes, and half spheres during daylight operation.

In general, evaporative losses from the solar pond surface are approximately 23 to 31% lower with the petri dishes and 15 to 28% lower with the half spheres when compared to the continuous plastic cover.

3.2 Effects of percent coverage on solar pond temperature evolutions

The effects of the continuous plastic cover at 99% coverage on the temperatures of the three zones of the solar pond are shown in Figure 20. A significant temperature increase near the surface occurs immediately after installation on February 11th, 2011 and is caused by the reduction of water and heat loss, from evaporation, at the surface [80]. The solar pond reaches a quasi-thermal steady-state on March 3rd, approximately 21 days after the start of the experiment. The temperatures in both the UCZ and NCZ increase for the 21-day time period. Temperatures in the LCZ did not rise significantly, likely due to the lower transmittance of the continuous cover (Figure 10). For this reason, other cover/element options were considered in order to improve evaporation suppression and to allow greater transmittance of radiation to the lower zones of the pond.

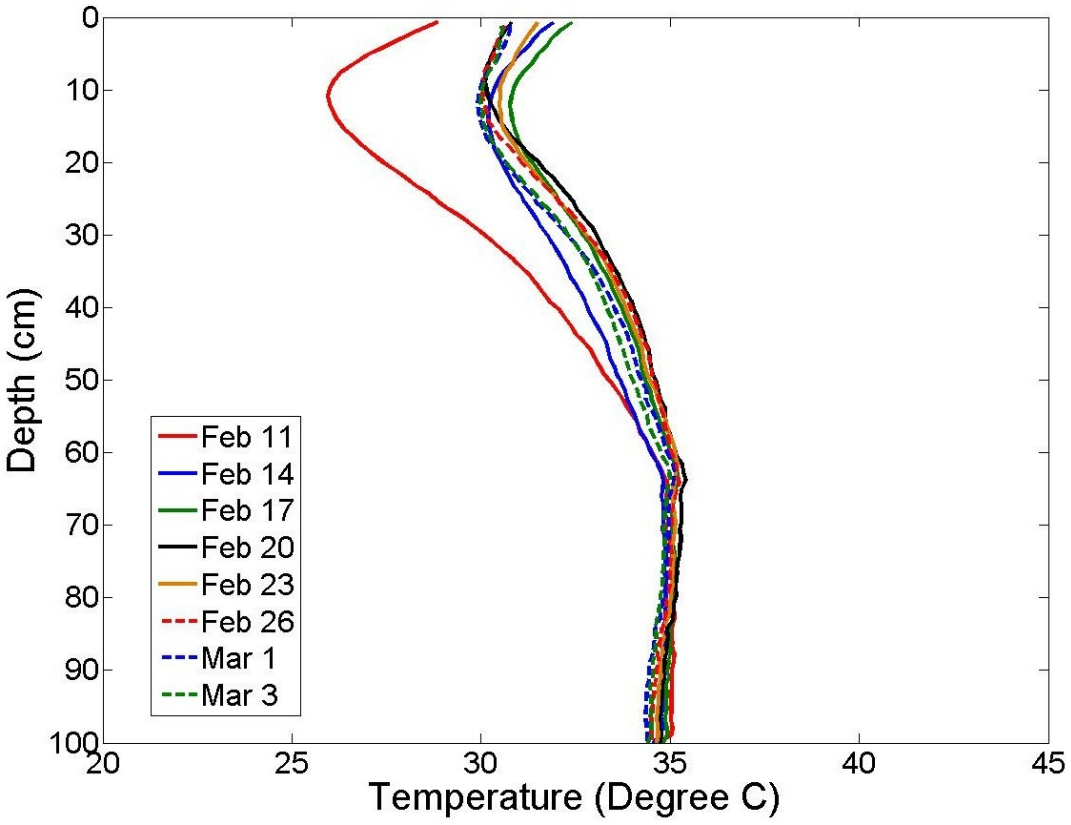

Figure 20: Temperature evolution of the fully covered (99%) solar pond with the continuous plastic cover.

In Figure 21, temperature profiles using petri dish and half sphere evaporation suppression elements are compared with the temperature profile for the continuous plastic cover experiment. The thermal quasi steady-states reached in the solar pond for each percent coverage tested for the continuous plastic cover is shown in Figure 21a. In general, this cover minimally affects both the LCZ and NCZ temperatures. However, temperatures in the UCZ generally increase with increasing percent coverage. Only a small volume of water is contained in the UCZ and, as a result, the amount of heat content provided by this zone only minimally affects the overall performance of the solar pond. Temperatures in the LCZ and NCZ are more

important than temperatures in the UCZ because heat extraction occurs in the LCZ, and is insulated by the NCZ above.

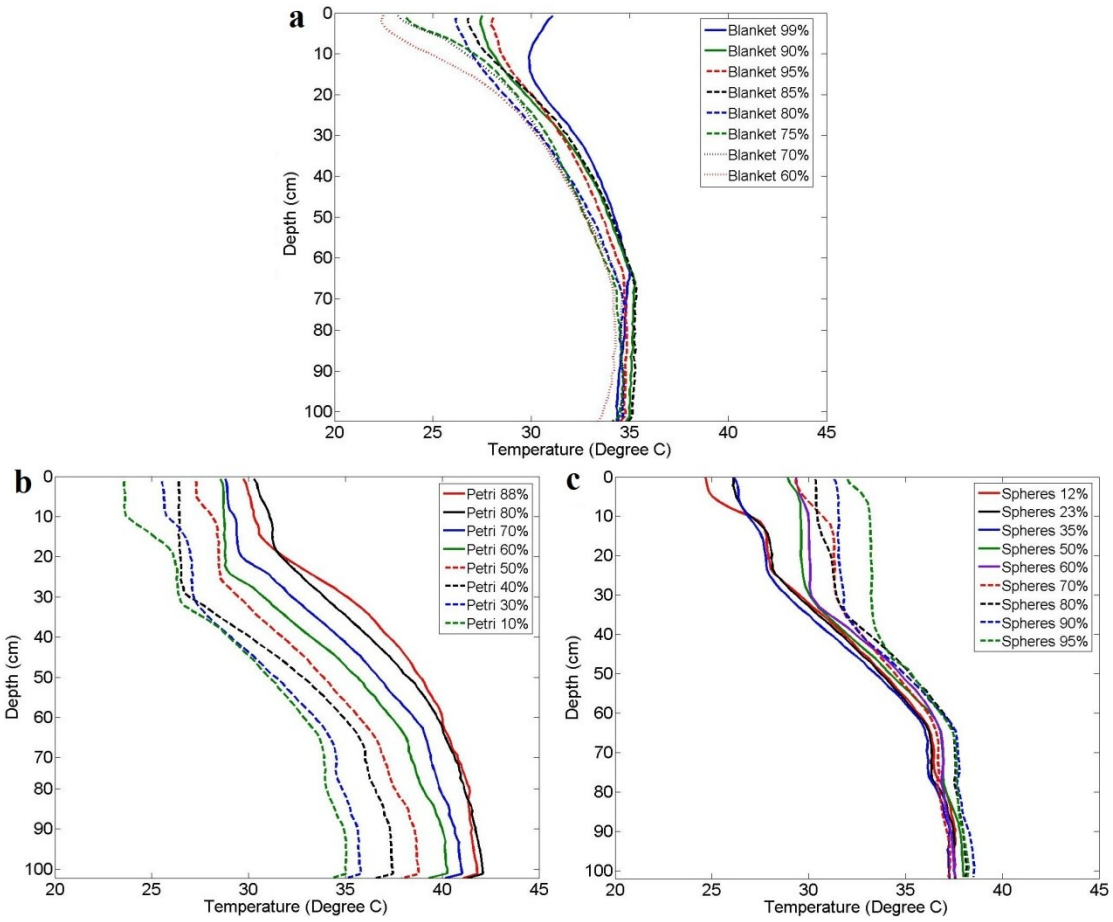

Figure 21: Overall solar pond temperature for each coverage percentage for: a) the continuous plastic cover, b) the petri dishes, and c) the half spheres.

The thermal-quasi steady-states reached in the solar pond for each percent coverage tested with the petri dishes is shown in Figure 21b. Unlike the continuous plastic cover, the effects of increasing percent coverage with the petri dishes can clearly be seen throughout the solar pond; clear increases in temperature occur in all zones. Because the petri dishes are completely transparent (Figure 10), they allow greater radiation penetration, specifically in the visible region, and thus, a higher temperature in the solar pond than the continuous plastic cover.

The thermal-quasi steady-states reached in the solar pond for each percent coverage tested with the half spheres is shown in Figure 21c. As percent coverage increases, higher temperature variations are observed in the UCZ, with only minimal changes observed in the LCZ. These temperature results are similar to the continuous plastic cover experiment, and were not anticipated when simply considering radiation penetration of the half sphere material (Figure 10). The discrepancy is likely due to the shape of the half sphere; the convex shape of the half sphere results in light and radiation scattering [81], reducing the amount of radiation that enters the solar pond. Air, which is a poor medium for heat transfer, is contained inside the half sphere (between the top of the half sphere and the water surface) and likely causes increased heat losses from the surface of the solar pond.

Comparison of 80% coverage between each of the three covers/elements shows that the petri dishes result in a 6 °C increase in average solar pond temperature over the continuous plastic cover and approximately a 3.5 °C increase over the half spheres. The petri dishes allow a maximum temperature of 43 °C to be reached in the LCZ at 88% coverage. Of the four data series shown in Figure 10, water allows the highest percent of radiation penetration and is generally higher than all three covers/elements over the visible spectrum. However, all three covers/elements perform better than no covers/elements with respect to increased temperature throughout the solar pond. Therefore, the loss of heat and water from the surface of a solar pond plays a greater role on overall temperature than the amount of radiation penetration through the surface. The use of less transmissive covers (i.e., continuous plastic cover) results in higher temperatures than an uncovered solar pond.

3.3 Effects of percent coverage on solar pond heat content

The heat content of the solar pond with respect to percent coverage of the surface for the three covers/elements is shown in Figure 22. In general, heat content for all three covers/elements increases as percent coverage increases; these increases in heat content are due to reduced evaporative losses and increased temperatures throughout the solar pond. The solar pond covered with petri dishes experiences a slight decrease in heat content from no coverage to 10% coverage, and the solar pond covered with half spheres experiences a slight decrease in heat content from 11% to 22% coverage. Following these decreases, heat content sharply increases for both elements. For all tested percent coverages of the solar pond, the continuous plastic cover results in lower heat content values when compared to the petri dishes and half spheres.

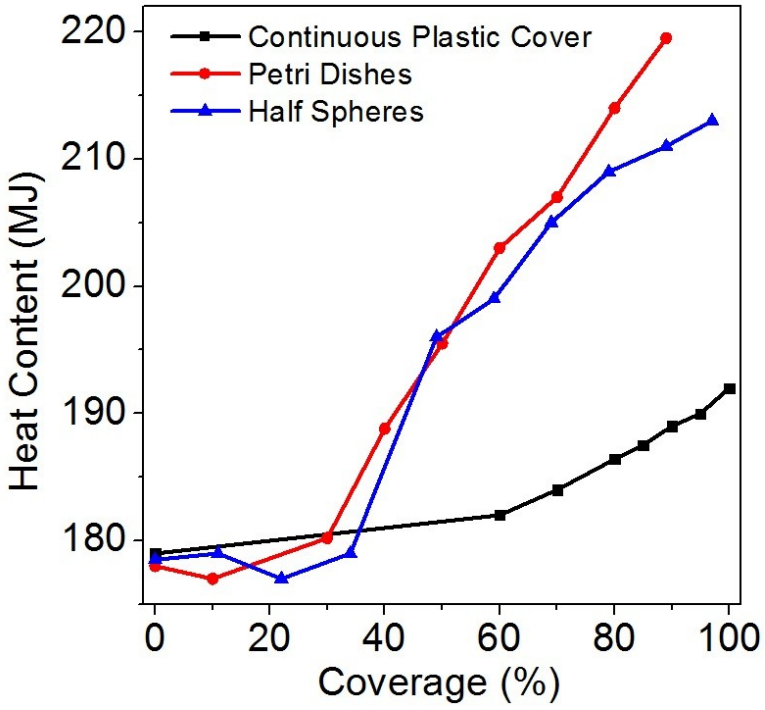

Figure 22: Solar pond heat content as a function of varying percent coverage with the continuous plastic cover, petri dishes, and half spheres.

The solar pond has a heat content of approximately 220 MJ at maximum coverage (88%) of the petri dishes and a heat content of approximately 213 MJ at maximum coverage (97%) of the half spheres. These maximum heat contents are comparable (3% difference); however the petri dishes achieve this heat content with approximately 9% less coverage of the solar pond.

3.4 Selection of most effective solar pond cover/element

From the results of the evaporation suppression experiments, the continuous plastic cover at 99% coverage offers the highest evaporation suppression, bringing the minimum evaporation rate to 0.60 mm per day from 5.1 mm per day. However, the continuous plastic cover also results in the lowest temperatures and lowest heat content values in the solar pond. Although the continuous plastic cover can almost completely suppress evaporation at 99% coverage, this percent coverage will be difficult to obtain in field applications on larger sized solar ponds. As a result, this type of cover is not considered practical for full-scale field applications.

When considering the reduction of evaporative losses from the solar pond surface during daylight operations for all percent coverages less than 99%, the petri dishes and half spheres outperform the continuous plastic cover significantly. Full coverage of the solar pond with the petri dishes (88% coverage) reduces surface evaporative losses by more than 51%, bringing the minimum evaporation rate to 2.50 mm per day. Full coverage of the solar pond with the half spheres (97%) reduces surface evaporative losses by more than 57%, bringing the minimum evaporation rate to 2.19 mm per day.

When the solar pond was covered with maximum coverage of petri dishes and half spheres, the respective maximum heat contents were similar (219 MJ and 213 MJ for the petri dishes and half spheres, respectively). However, for the solar pond covered with petri dishes, the maximum temperature in the LCZ was 43 °C and for the solar pond covered with the half spheres, the maximum temperature in the LCZ was 38 °C.

Therefore, although coverage with the petri dishes results in a 12% higher evaporation rate, the solar pond covered with the petri dishes has higher LCZ temperatures and higher heat contents than the solar pond covered with the half spheres. Ultimately, the petri dishes perform the best of the three covers/elements tested since they result in the highest temperature increase in all three layers and low evaporative losses, both of which contribute to achieving the highest heat content in the solar pond. Using the best case scenario from the evaporation reduction experiments (88% coverage with petri dishes), the average water loss from the surface of the solar pond is calculated to be 2.00×10^{-3} m^3 of freshwater per m^2 of solar pond surface area per day.

3.5 Effects of evaporation suppression and increased heat content on freshwater production from the coupled SGSP/DCMD system

3.5.1 SGSP/DCMD experimental results

The coupled SGSP/DCMD system achieved a maximum water production rate of 2.41×10^{-3} m^3 of freshwater per m^2 of solar pond surface area per day. Thus, the coupled SGSP/DCMD system achieves an average positive net water production of 0.41×10^{-3} m^3 freshwater per m^2 of solar pond surface area per day when

evaporative losses from the solar pond surface are suppressed by the petri dishes (88% coverage). The temperature difference across the membrane in this study was 12 °C and membrane surface area was 0.015 m^2.

Previous experimental work reported a maximum water production rate of 1.16 x 10^{-3} m^3 freshwater per m^2 of solar pond surface area per day from the coupled SGSP/DCMD system using hollow fiber membranes [82]. The membrane in that case had an area of 0.1 m^2; thus, the ratio of the membrane area to the solar pond surface area was 20 times larger. In that case, water loss due to evaporation was higher than water production from the DCMD system, and net water production was negative. The temperature difference across the membrane was 9 °C. The lower water production in this study is attributed in part to the low ratio of solar pond surface area-to-membrane surface area, which in this case was 200 to 0.1 m^2, or 20. Knowing that the ideal ratio is 1000 [1], improved efficiencies were expected in the current study where the ratio is 200 to 0.015 m^2, or 134.

The maximum water production rate for a multi-flash system combined with an operational solar pond in El Paso, Texas was 1.60 x 10^{-3} m^3 of freshwater per m^2 of solar pond surface area per day [83]. However, evaporative losses from the solar pond surface were not considered. Also, this production rate was enhanced by high operating temperatures and pressures (temperature greater than 60 °C in the feed and a pressure of 30 kPa) [26]. The same solar pond in El Paso was also tested with an AGMD system using a temperature difference across the membrane of 41 °C. In that case, a water production rate of 0.16 x 10^{-3} m^3 of freshwater per m^2 of solar pond

surface area per day was reported [27]. Once again, evaporative losses from the solar pond surface were not considered.

The maximum water production achieved during 24-hour light operation of the solar pond was 2.89 x 10^{-3} m^3 of freshwater per m^2 of solar pond surface area per day. In this scenario, a maximum temperature of 53 °C was achieved in the LCZ (Figure 23). Water from the LCZ was extracted at approximately 65 cm depth, passed through a heat exchanger, and was reinjected at approximately 81 cm. After 24 hours of DCMD operation, a maximum temperature of 47 °C was observed in the LCZ. Even with 24-hour light operation, the laboratory solar pond LCZ temperature decreased approximately 6 °C during daily operation of the coupled DCMD system. Therefore, heat extraction from the laboratory solar pond for DCMD operation needs time to recover between DCMD operations and cannot be operated 24 hours a day. The temperature in the LCZ during 24-hour light operation with petri dishes is higher than previous tests performed on the same solar pond [82]. Full-scale operation using a large solar pond surface area and with a solar pond surface area-to-membrane surface area approaching 1000 would likely enable 24-hour solar pond operation at steady-state.

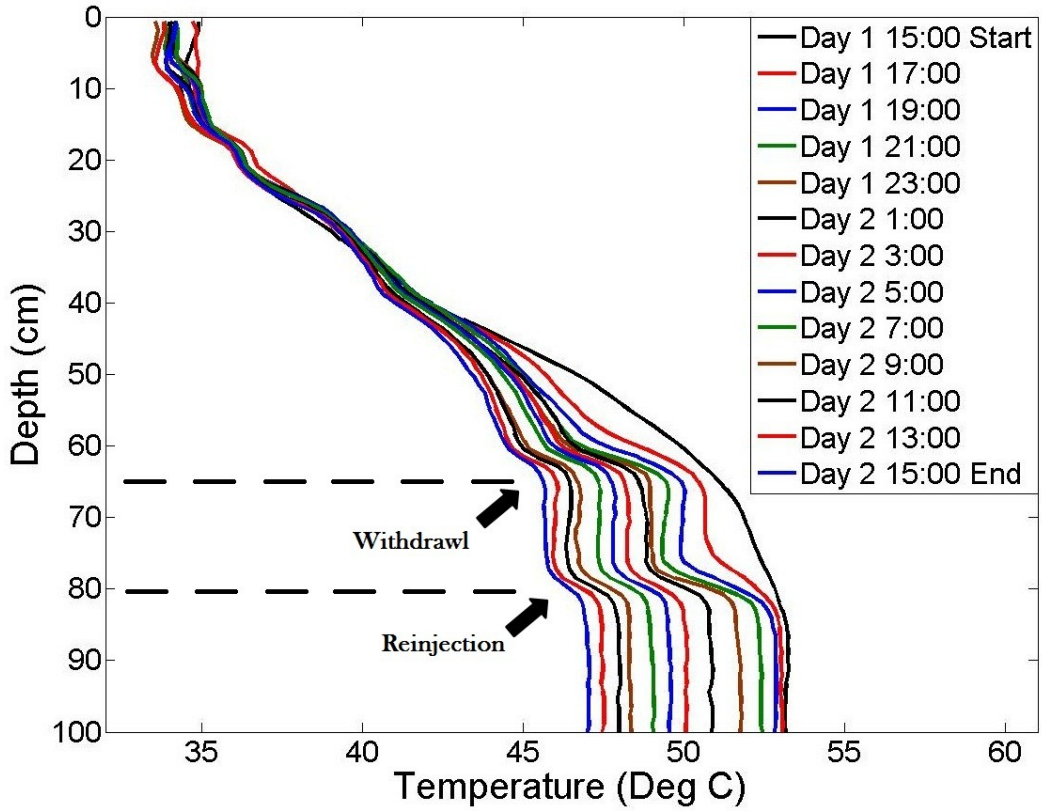

Figure 23: Temperature evolution of the laboratory solar pond with 24-hour light operation and DCMD heat extraction.

3.5.2 DCMD model results

Using the measured experimental temperature difference (12 °C) across the membrane surface, the DCMD model predicted a water production rate of 2.63 x 10^{-3} m^3 of freshwater per m^2 of solar pond surface area per day. This rate does not account for evaporative losses from the surface of the solar pond. When the experimental rate for evaporative loss of 2.00 x 10^{-3} m^3 of water per m^2 of solar pond surface area per day is considered, the modeled production rate (0.63 x 10^{-3} m^3 of freshwater per m^2 of solar pond surface area per day) is approximately 35% higher than the experimental production rate; this lower rate of the actual system is most likely due to inefficiencies such as heat loss through tubing and temperatures measured at the inlet

rather than the membrane surface. The water production predictions for the coupled SGSP/DCMD system are higher than earlier modeling results due to the increase in temperature in the NCZ and the LCZ.

This is consistent with previous modeling by Suarez et al. [1] that predicted production of 1.58 x 10^{-3} m^3 of freshwater per m^2 of solar pond surface area per day from the coupled SGSP/DCMD system with a different membrane module. However, net water production for that study is negative when the surface evaporation rate of 4.08 x 10^{-3} m^3 of freshwater per m^2 of solar pond surface area per day is considered. Additionally, a modeled production rate of 2.70 x 10^{-3} m^3 of freshwater per m^2 of solar pond surface area per day was reported with construction of the SGSP within the lake [1]. Both the experimental and modeled freshwater production rates of a separate SGSP utilizing covers/elements compare favorably with the modeled rate of an SGSP built inside the lake. This is due to the increase in heat content of the solar pond and, more specifically, the increase in temperature of the LCZ.

3.6 Bench-scale DCMD scaling experiments

3.6.1 CHEMCHAU analysis

From the unpublished results presented in section 1.5.2, hydromagnesite and calcite were found to be supersaturated in the solution and hydromagnesite was found to precipitate at a molar rate that was 30 times more than calcite. As Walker Lake water was concentrated to more than 90%, other minerals began precipitating, including thenardite, thermonatrite, and halite. The precipitants predicted from CHEMCHAU during the concentration of Walker Lake water can be used to predict

possible scalants that could form during distillation of Walker Lake water in the coupled SGSP/DCMD system.

3.6.2 OLI Analyzer Studio 3.2 analysis

An isothermal composition survey from 0 to approximately 99% concentration of Walker Lake water predicted that hydromagnesite and calcite, both at supersaturation, are the first to precipitate (Figure 24), which agree with the CHEMCHAU model. Additionally, Analyzer Studio 3.2 predicts that hydromagnesite precipitates at a rate of 25 times that of calcite, which also generally agrees with CHEMCHAU. Nahcolite ($NaHCO_3$), halite, and thenardite are also predicted to precipitate out of solution at 95%, 98%, and 99% concentration, respectively. Therefore, nahcolite, halite, and thenardite precipitates are not expected to form in the NCZ and LCZ since Walker Lake water will not be concentrated more than 90% during filling or daily operation. However, after 95% concentration, halite is predicted to precipitate at a molar rate 37 times that of hydromagnesite, and over 200 times that of calcite.

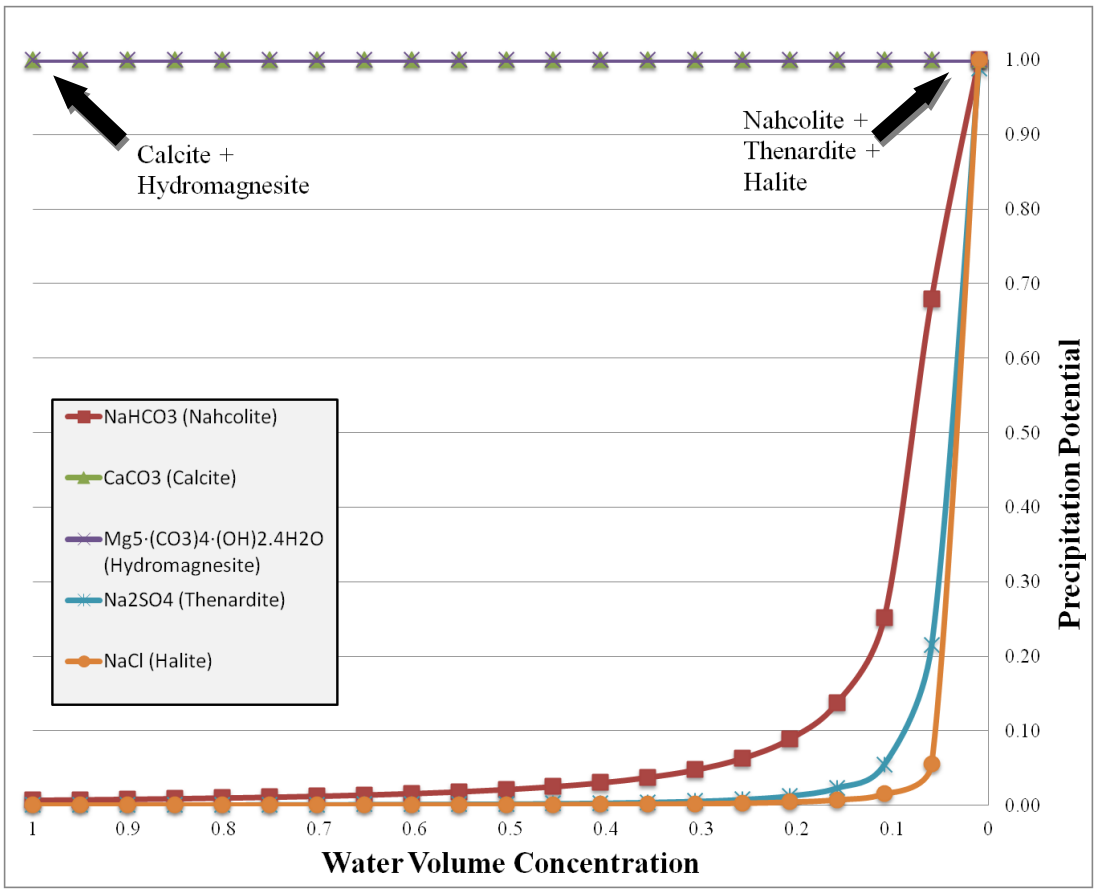

Figure 24: Precipitants that form as Walker Lake water is concentrated by evaporation at 45 °C using Analyzer Studio 3.2 model. Arrows point to precipitation of calcite ($CaCO_3$), hydromagnesite [$Mg_5{\cdot}(CO_3)_4{\cdot}(OH)_2{\cdot}4H_2O$], nahcolite ($NaHCO_3$), thenardite ($Na_2SO_4$), and halite (NaCl).

3.6.3 Comparison of results from CHEMCHAU and OLI Analyzer Studio 3.2 models

CHEMCHAU and Analyzer Studio 3.2 predict that Walker Lake is supersaturated with hydromagnesite and calcite and predict similar rates of precipitation for hydromagnesite, calcite, and halite. Both models also predict precipitation of thenardite and halite at higher concentrations. However, CHEMCHAU predicts thermonatrite precipitation at higher concentrations, while Analyzer Studio 3.2 predicts nahcolite precipitation at higher concentrations.

Discrepancies are expected in the results of the models with respect to possible precipitants and concentrations at which precipitants will form since the models rely on different data sets and use different calculation mechanisms: CHEMCHAU uses the PITZER equations [51] while Analyzer Studio 3.2 uses the Helgeson equation of state [75].

3.6.4 Experimental scaling of MD membranes

During desalination of Walker Lake water with DCMD, when the bulk concentration is 92%, the feed concentration at the membrane surface approaches 99% due to concentration polarization; at this concentration the following scalants are possible based on modeling results: hydromagnesite, calcite, halite, thermonitrate, nahcolite, thenardite, and/or thermonitrate. Results from bench-scale DCMD experiments are shown in Figure 25 and were conducted to confirm the precipitants that form. Both DCMD flux (black) and feed concentration (red) are shown with respect to time. As vapor from the feedwater permeates through the membrane, the feed tank solution becomes more concentrated. Additionally, as the flux declines, the slope of the concentration line becomes more horizontal because the rate of water loss from the feed tank decreases. Both models predict that at 90% concentration the feedwater is saturated with hydromagnesite and calcite. Flux decline is likely occurring as a result of the precipitation and scale formation of hydromagnesite and calcite on the membrane surface. For this reason, cleaning cycles were initiated after the flux declined below 10% of the initial flux (at 3000 and 7300 minutes). After the second cleaning cycle, the experiment continued until the feed volume was less than 10% of the initial volume, or more than 90% concentration of the feedwater.

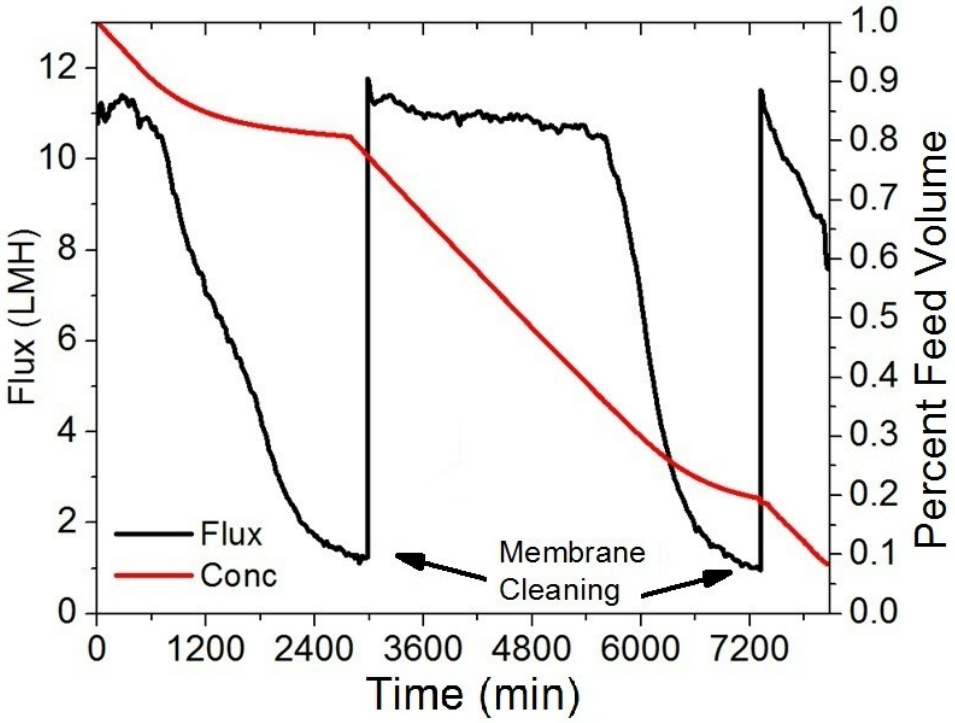

Figure 25: DCMD flux decline experiment. Permeate flux declines as the feed is concentrated and the volume decreases. Citric acid solution was recirculated over the membrane when flux declined below 10% of the initial flux in order to remove scalant from the membrane surface. Cycles were performed at 3000 and 7300 minutes in order to reduce the volume of feedwater to 10% of the original.

3.6.5 Scanning electron microscope and energy dispersive spectrometry

SEM images of the surface of a virgin membrane are shown in Figures 26a, b, and c using three magnifications: 500x, 5000x, and 10,000x, respectively, and SEM images of the surface of a membrane after scaling experiments (as in Figure 25) are shown in Figures 26d, e, and f at the same magnifications. Comparison of the virgin and scaled membrane samples shows that nearly the entire surface of the polymeric membrane is covered with a crystal structure after scaling. The scale on the fouled membrane samples (Figures 26d, e, f) has little similarity to SEM images in the literature [54, 55, 84-86] for calcite and dolomite (a combination of calcium and magnesium carbonates) crystals. However, compared to SEM images of magnesite in

literature [87], the scale on the fouled membrane shows some structural similarities. No images of hydromagnesite were found.

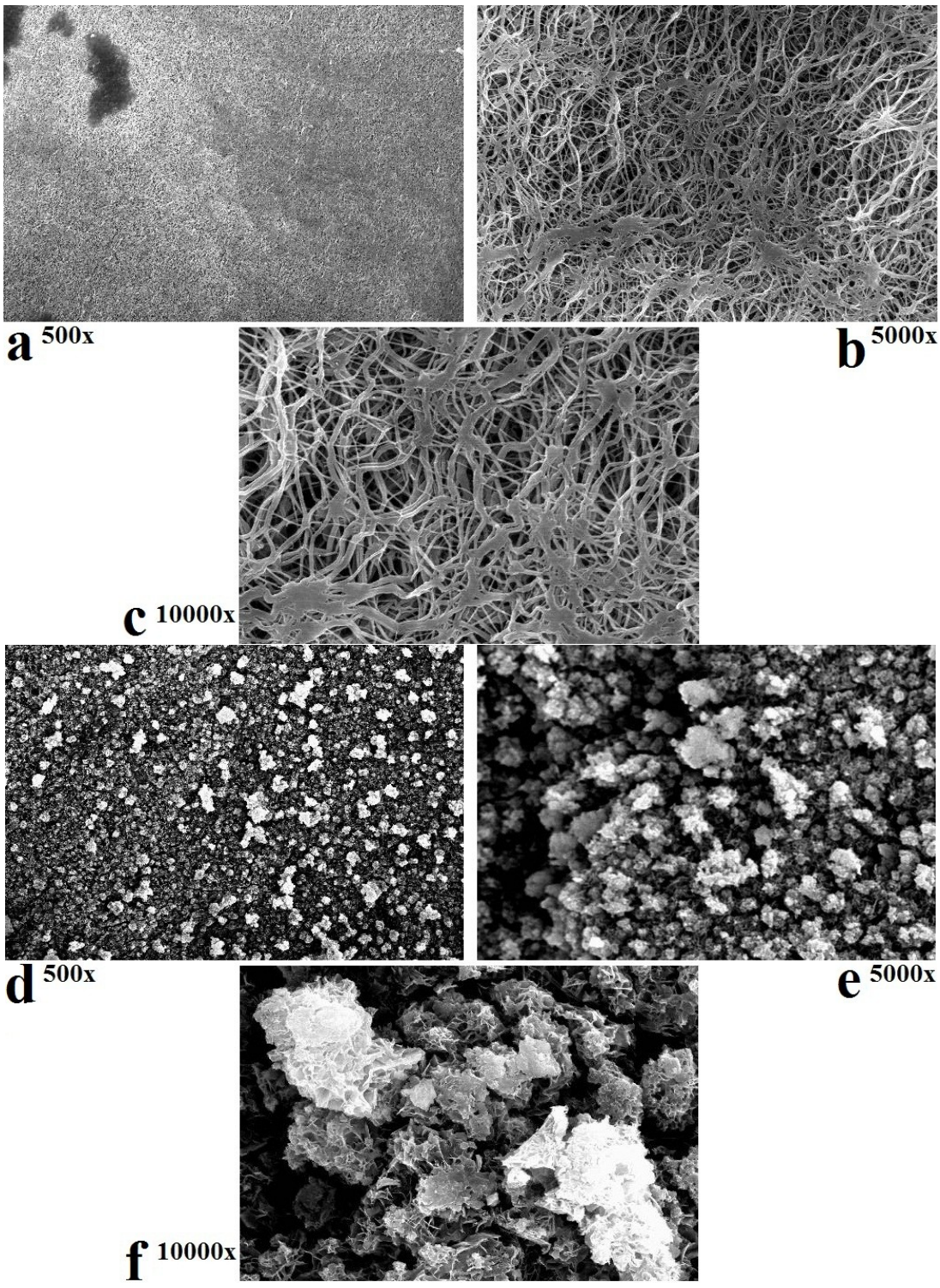

Figure 26: a, b, and c show a virgin membrane sample viewed under three different magnifications with SEM, while d, e, and f show a fouled membrane sample viewed under three magnifications.

Results from the EDS scan performed on both membrane samples are shown in Table 5; atomic percentages of the chemical polytetrafluoroethylene (PTFE) formula and atomic percentages of the elements present on the virgin and fouled membranes are given. The fouled membrane has much less fluorine than the virgin membrane, which suggests that the surface of the fouled membrane is obscured from the EDS laser by scale. The presence of sodium and chlorine indicate possible halite, nahcolite, and/or thenardite scale. The presence of carbon, oxygen, and magnesium indicate possible magnesite or hydromagnesite scale, and specifically, the carbon present may suggest carbonate scale. The carbon-fluorine ratio on the fouled membrane is higher than the carbon-fluorine ratio on the chemical PTFE or virgin membrane sample.

Table 5: Atomic percentages of the elements in the chemical polytetrafluoroethylene (PTFE) formula, and atomic percentages of the elements present on the virgin and fouled membranes measured with EDS.

Element	Chemical PTFE $(C_2F_4)_n$			Virgin Membrane			Fouled Membrane		
Carbon	24.02	±	0.00	28.75	±	0.54	19.72	±	2.96
Oxygen							42.13	±	4.10
Fluorine	75.98	±	0.00	71.25	±	0.76	17.01	±	5.10
Sodium							11.25	±	2.75
Magnesium							5.86	±	1.68
Sulfur							0.83	±	0.14
Chlorine							2.83	±	1.12
Potassium							0.20	±	0.09
Calcium							0.17	±	0.08
Total	100.00	±	0.00	100.00	±	1.30	100.00	±	18.02

Additionally, the presence of calcium suggests that calcite is most likely scaling on the membrane surface. However, the amount of calcium is significantly less than the amount of magnesium, as magnesium is present on the membrane surface approximately 35 times more than calcium. These results confirm both the CHEMCHAU and Analyzer Studio 3.2 results that showed hydromagnesite precipitating at higher rates than calcite.

3.6.6 X-ray diffraction confirmation of scalant

Results from XRD analyses of the scale removed from the membrane samples are shown in Figure 27a, b, and c. the XRD scan with known hydromagnesite (blue) and halite (red) peaks are graphed in Figure 27a, known calcite (blue), magnesite (red), and brucite (magenta) peaks are graphed in Figure 27b, and known nahcolite (red), sodium sulfate (green), dolomite (magenta), and sodium carbonate (blue) peaks are graphed in Figure 27c. All of the major hydromagnesite and halite peaks from the scale match the known data, suggesting that the scale is likely a combination of these two compounds. None of the calcite, magnesite, brucite, nahcolite, sodium sulfate, dolomite, or sodium carbonate peaks from the scale match the known data, eliminating the possibility that the scale consists of these compounds. Therefore, it can be deduced with a high degree of certainty that the scale consists of both hydromagnesite and halite crystals.

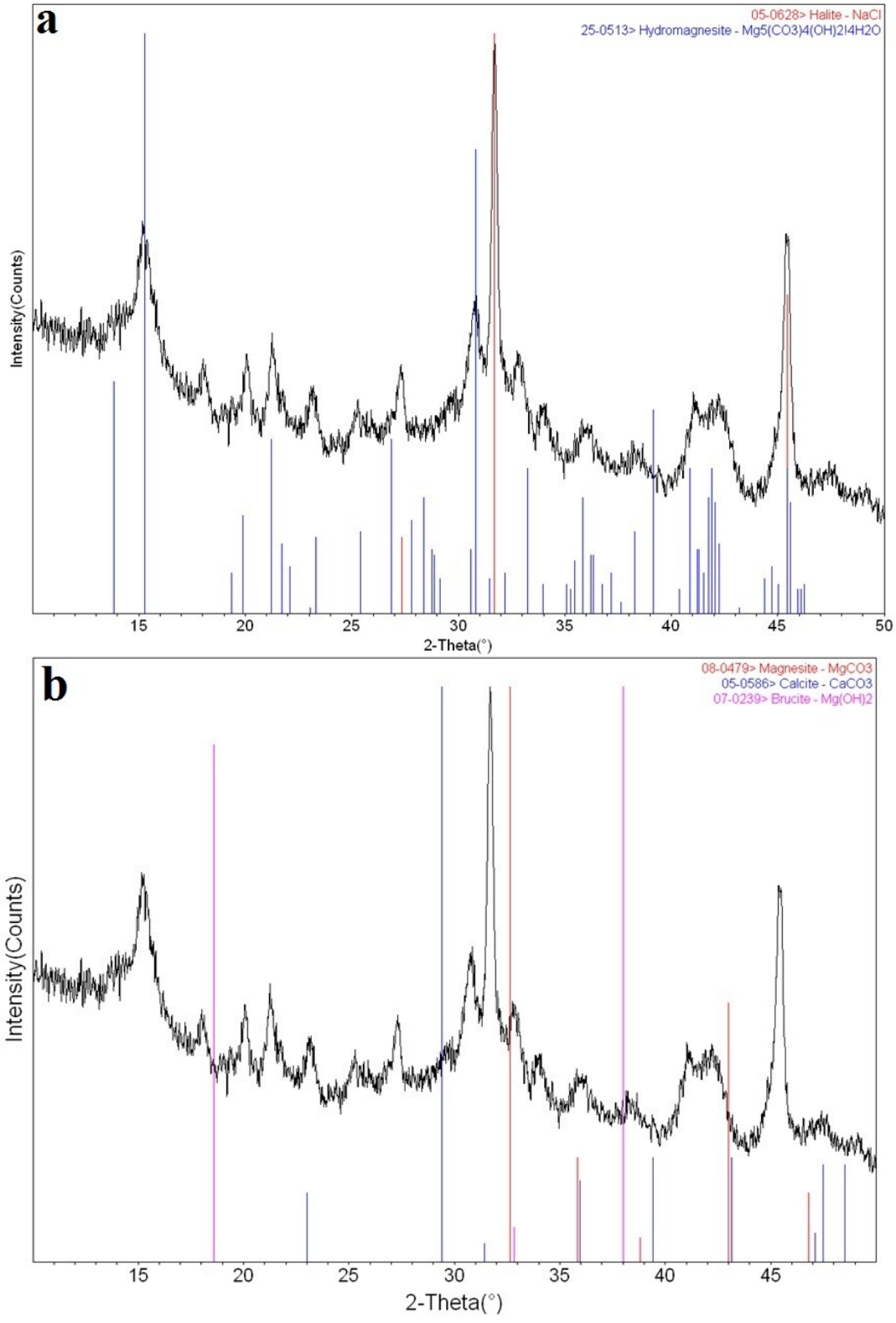
a
05-0628> Halite - NaCl
25-0513> Hydromagnesite - Mg5(CO3)4(OH)2I4H2O
Intensity(Counts)
15
20
25
30
35
40
45
50
2-Theta(°)
b
08-0479> Magnesite - MgCO3
05-0586> Calcite - CaCO3
07-0239> Brucite - Mg(OH)2
Intensity(Counts)
15
20
25
30
35
40
45
2-Theta(°)

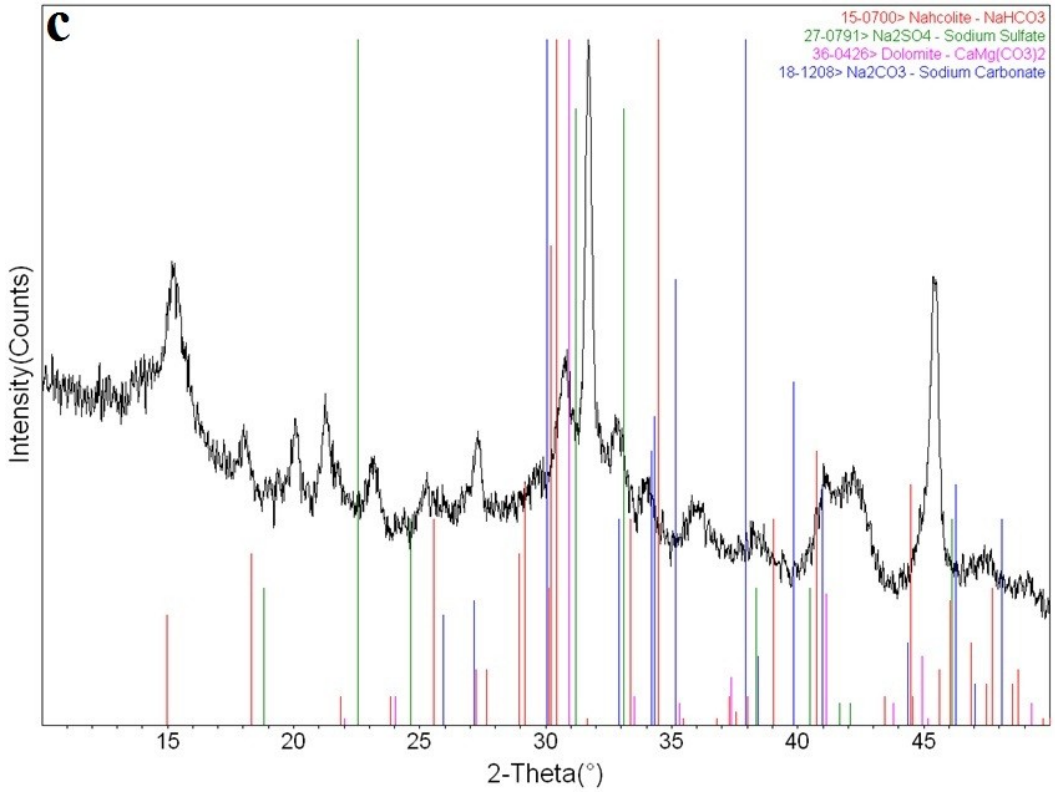

Figure 27: X-ray diffraction scans with known peaks of a) hydromagnesite (blue) and halite (red), b) magnesite (red), calcite (blue), and brucite (magenta), and c) nahcolite (red), sodium sulfate (green), dolomite (magenta), and sodium carbonate (blue).

The presence of hydromagnesite compounds was consistent with the results of both models which predicted Walker Lake feedwater to be saturated with hydromagnesite. Halite was also predicted as a potential by both CHEMCHAU and Analyzer Studio 3.2 after 98% concentration of the feedwater. However, it is likely that halite is seen at 92% concentration because of concentration polarization at the membrane surface. Concentration polarization occurs when water permeates through the membrane, causing solute concentrations to increase at the membrane surface as the bulk concentration remains the same [88]. Effects of concentration polarization may have resulted in the concentration of the feedwater at the membrane surface surpassing 98%, while the bulk concentration remained near 90%. Because

CHEMCHAU and Studio Analyzer 3.2 simulate ideal evaporators, concentration polarization as it occurs in DCMD is not considered. Therefore, DCMD cannot be modeled strictly as an ideal evaporator where water is removed through evaporation by heating alone because both temperature and concentration polarization affect the feed solution at the membrane surface.

Similar to hydromagnesite, Walker Lake feedwater is saturated with calcite; however, calcite was not detected in the scalant by XRD. It is likely that calcite formed on the membrane surface in low concentrations, but is not seen by XRD when compared to the higher concentrations of both hydromagnesite and halite. Modeling results by Analyzer Studio 3.2 predicted halite precipitation at a rate 37 times greater than hydromagnesite and over 200 times greater than the rate of calite. The lack of calcite detected in the scalant has also been found in previous studies using feedwater saturated with calcite [53, 57, 59, 60].

3.7 Membrane cleaning cycles

The recorded flux (black), feed temperature (red), and permeate temperature (blue) with respect to time are shown in Figure 28 for a DCMD desalination experiment. The feed and permeate temperatures were maintained near 45 and 25 °C, respectively. After approximately 2500 min, the flux dropped to approximately 10% of the initial flux and a chemical cleaning cycle with Na_2EDTA/NaOH was initiated. Approximately 92% flux recovery was achieved by the cleaning, indicating that scale was sufficiently removed from the membrane surface by the Na_2EDTA/NaOH cleaning solution.

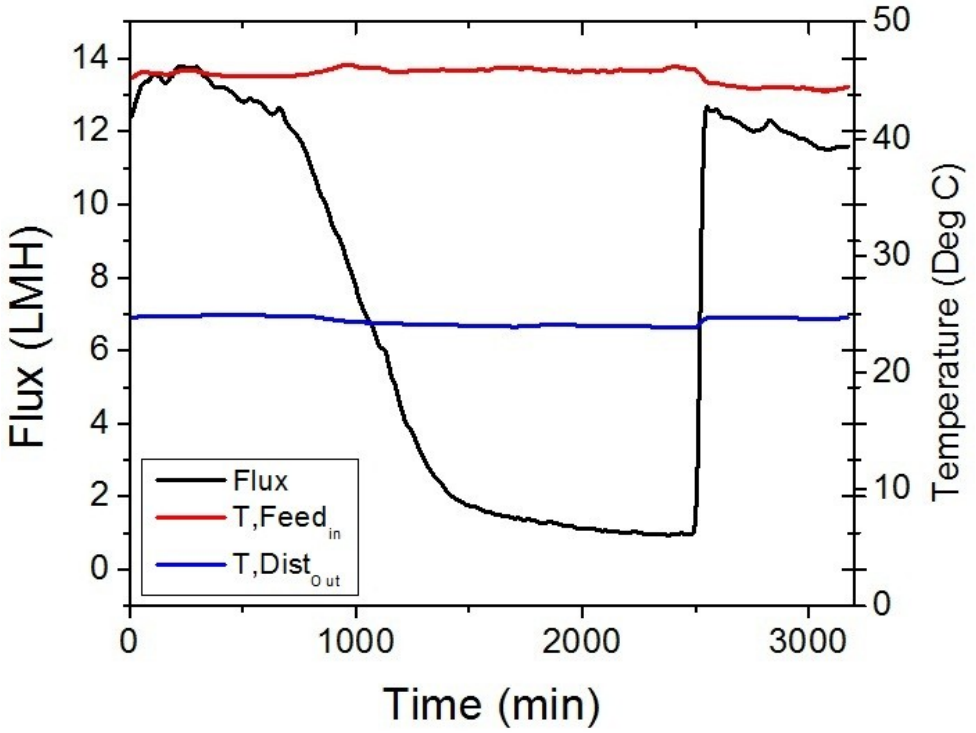

Figure 28: Membrane flux during a DCMD cleaning experiment. An Na_2EDTA/NaOH cleaning cycle was conducted after 2500 minutes. Feed and permeate temperatures were near 45 and 25 °C, respectively, and feed and permeate flow rates were 1.5 L/min.

A DCMD desalination experiment was then performed with a virgin membrane sample. Flux recovery after a citric acid cleaning cycle that occurred at approximately 3000 min is shown in Figure 29. Approximately 95% flux recovery was achieved by the cleaning, indicating that scale was sufficiently removed from the membrane surface by the citric acid cleaning solution.

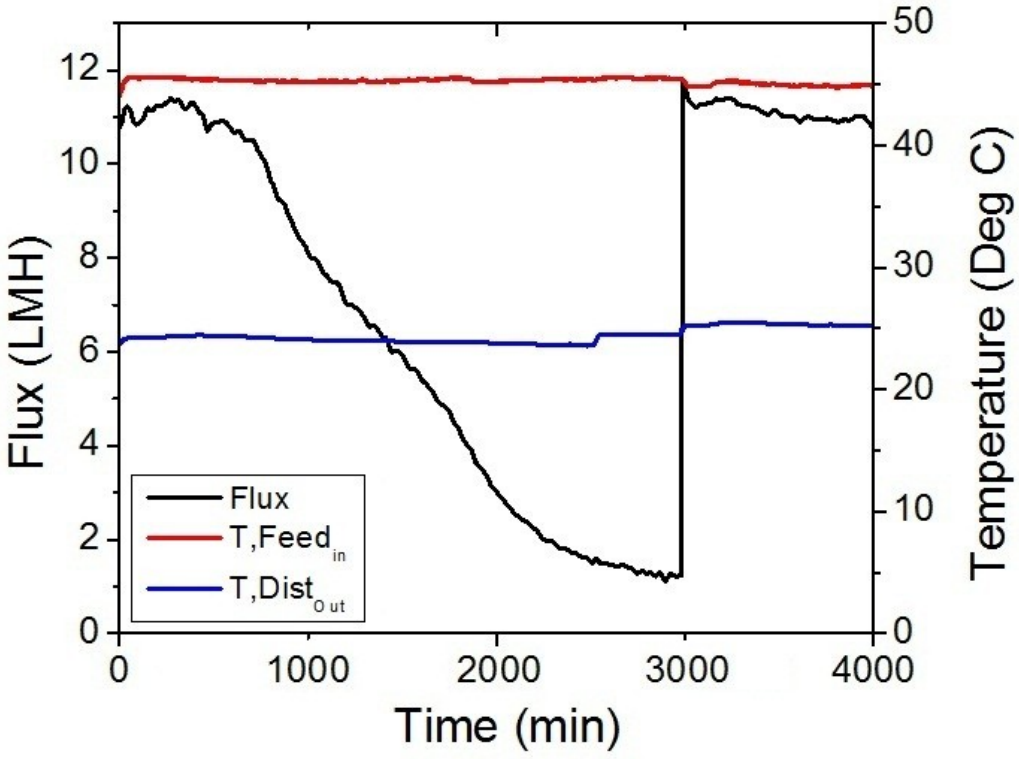

Figure 29: Membrane flux during a DCMD cleaning experiment. A citric acid cleaning cycle was conducted after 3000 minutes. Feed and permeate temperatures were near 45 and 25 °C, respectively, and feed and permeate flow rates were 1.5 L/min.

The membrane surface after cleaning with Na_2EDTA/NaOH is shown at three magnifications in Figure 30. At 500x magnification (Figure 30a), the surface of the cleaned membrane is free from the scale that was present on the fouled membrane (Figure 26d). When magnified to 10,000x (Figure 30c), the membrane appears to be nearly free of all scalant. Some deposits can be seen at 5000x (Figure 30b) magnification, suggesting that the Na_2EDTA/NaOH cleaning cycle did not achieve complete removal of scale. Additionally, the surface of the cleaned membrane at 10,000x magnification appears to be nearly identical to the virgin membrane (Figure 26c), suggesting the cleaning solution does not appear to damage or physically alter the membrane surface.

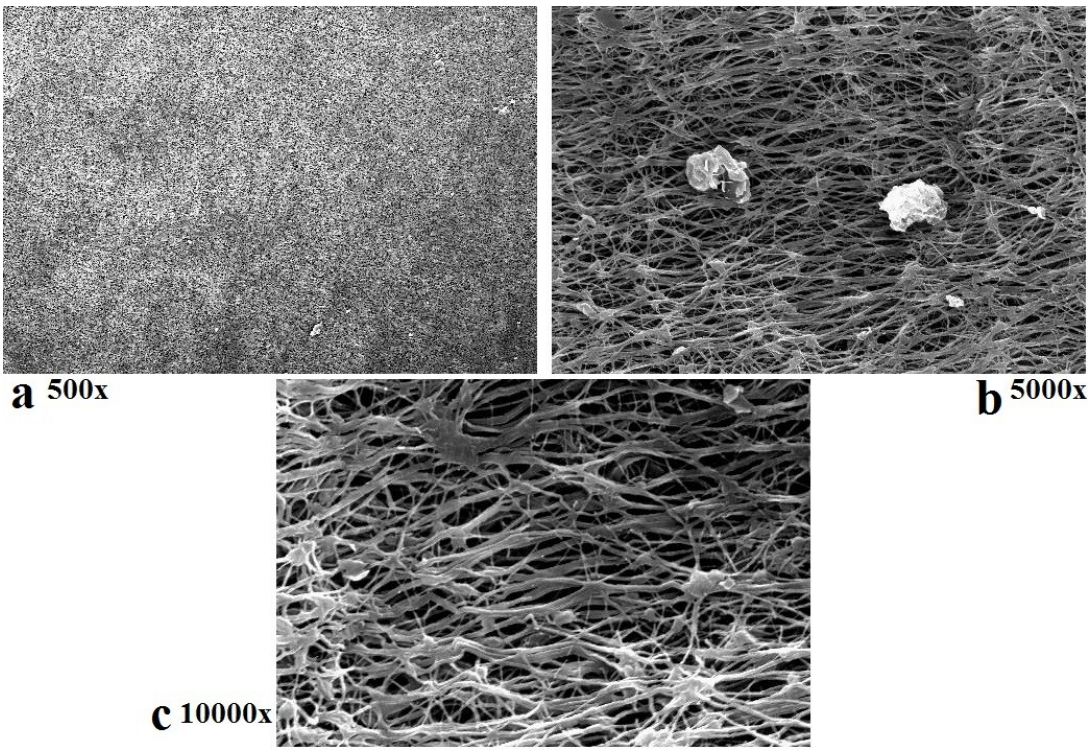

Figure 30: Membrane surface following Na_2EDTA/NaOH cleaning at a) 500x, b) 5000x, and c) 10,000x magnifications.

The membrane surface after cleaning with citric acid solution is shown at three magnifications in Figure 31. For all magnifications, the membrane appears to be free from scale. However, at both 5000x and 10,000x magnifications (Figure 31b and c), the polymeric structure of the membrane appears to differ from the virgin membrane (Figure 26b and c), suggesting that the citric acid cleaning solution may have altered the membrane surface. Membrane samples treated with multiple citric acid cleaning cycles were able to achieve flux recovery up to 95% while maintaining 99.9% rejection, thus the observed physical differences of the membrane surface do not appear to negatively impact membrane performance.

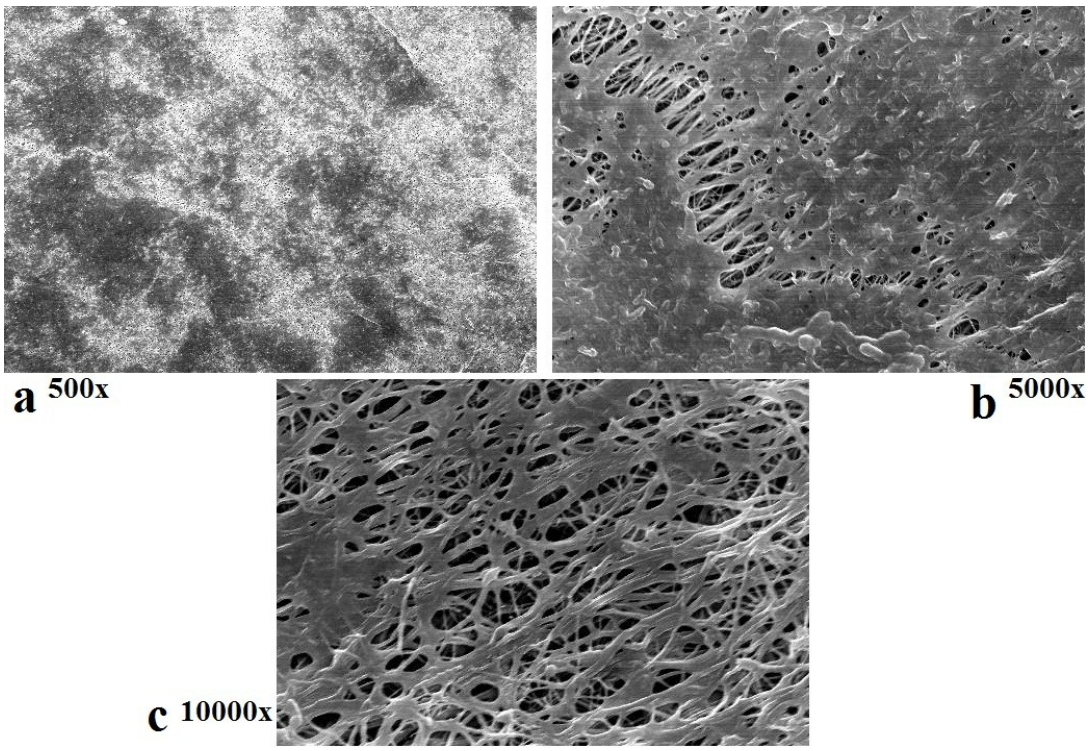

Figure 31: Membrane surface following citric acid cleaning at a) 500x, b) 5000x, and c) 10,000x magnifications.

Results from the EDS analysis in atomic ratio (the percentage of each atom to the total number of atoms detected during the analysis) are shown in Table 6 for each cleaned membrane surface along with the original fouled membrane surface, the virgin membrane surface, and the chemical PTFE formula. The elemental analyses show that the membrane cleaned with citric acid has a higher percentage of fluorine than the fouled membrane. Citric acid, a strong chelating agent, is able to remove both divalent cations (Mg^{2+} and Ca^{2+}), while Na_2EDTA, another strong chelating reagent, is only able to remove calcium, with very little removal of magnesium and oxygen (hydromagnesite). This was consistent with previous studies which demonstrated that EDTA effectively removed calcium [89]. Both cleaning solutions

recover the atomic ratios of fluorine, carbon, and oxygen that are associated with the virgin membrane surface.

Table 6: Elemental analyses of virgin, fouled, Na_2EDTA/ NaOH cleaned, and citric acid cleaned membranes. Additionally, the atomic percentage for a PTFE membrane is shown.

	Chemical PTFE	Virgin Membrane	Fouled Membrane	Citric Acid Cleaned	NaEDTA/NaOH Cleaned
Carbon	24.02 ± 0.00	28.75 ± 0.54	19.72 ± 2.96	28.85 ± 4.38	28.00 ± 4.30
Oxygen			42.13 ± 4.10	6.64 ± 0.45	6.38 ± 1.11
Fluorine	75.98 ± 0.00	71.25 ± 0.76	17.01 ± 5.10	57.14 ± 7.35	55.54 ± 10.66
Sodium			11.25 ± 2.75	4.54 ± 0.50	5.78 ± 0.23
Magnesium			5.86 ± 1.68	1.01 ± 0.78	1.90 ± 0.58
Sulfur			0.83 ± 0.14	0.00 ± 0.00	0.36 ± 0.00
Chlorine			2.83 ± 1.12	1.82 ± 0.12	1.93 ± 0.15
Potassium			0.20 ± 0.09	0.00 ± 0.00	0.10 ± 0.00
Calcium			0.17 ± 0.08	0.00 ± 0.00	0.00 ± 0.00
Total	100.00	100.00	100.00	100.00	99.99

4. Conclusions and Future Research

During this study, transparent floating elements and a continuous plastic cover were tested for suppression of evaporation from the solar pond. Of the covers/elements tested, petri dishes were the best evaporation suppression element due to their transmissivity, low refraction of radiation, and ease of installation. Suppression of evaporative losses from the solar pond surface also resulted in increased temperatures throughout the solar pond and increased overall solar pond heat content. The investigation of transparent covers/elements is unique from previous studies in ponds where increasing temperature and heat content are not desired. Covers/elements are also expected to have the additional benefit of decreasing wind-driven mixing across the surface of the solar pond [90, 91]. Reducing wind-driven mixing decreases the necessary depth of the UCZ which, as a result, increases the depth of the NCZ. The increase in NCZ thickness would create a larger insulating layer that would allow the LCZ to store more heat [92]. The combined loss of heat and water from the surface of the solar pond results in higher operating efficiencies.

Two models were used to predict the precipitants that would likely form during concentration of Walker Lake water to fill the SGSP and during DCMD concentration. Hydromagnesite and calcite were predicted to form during concentration of Walker Lake water. The main scalants predicted to form during DCMD operation were hydromagnesite and calcite. Hydromagnesite and halite were found to be the main scalants on the membrane surface. Halite most likely formed

due to concentration polarization at the membrane surface; small quantities of calcite were also likely present although not detected.

Cleaning cycles were conducted when the DCMD flux dropped below 10% of the original flux during concentration of Walker Lake feedwater. Flux recoveries of approximately 94% were achieved using citric acid or EDTA cleaning solutions. The citric acid cleaning solution performed slightly better than the EDTA cleaning solution in terms of flux recovery and removal of scalant (as observed by SEM). In addition to SEM, EDS, and XRD analyses were performed in order to determine the magnitude of scale deposit and the type of scalant present.

The proposed coupled SGSP/DCMD system was found to be feasible for terminal lake reclamation when utilizing floating elements to suppress evaporation and cleaning cycles to remove membrane scale and restore flux across the membrane. Positive freshwater production rates from the coupled SGSP/DCMD system, which have not been achieved in previous coupled systems, were achieved in this investigation.

Future research for the reclamation of Walker Lake using a combined SGSP/DCMD system should be mainly focused on the practicality of building the proposed treatment system in the field. A comparison of an external solar pond, as shown in this study, versus a solar pond built inside the lake should be made. The feasibility of year-round operation for both cases should be evaluated, as well as the actual evaporative losses and radiation available for collection at Walker Lake. The rate of freshwater production as well as the disposal of excess concentrate should also be taken into account. Finally, selection of the DCMD membrane and module and

selection of the SGSP cover/element should be carefully considered. It is critical to select membranes and covers/elements that maintain their integrity when exposed to field operating conditions.

5. References

[1] F. Suarez, S. Tyler and A.E. Childress, A theoretical study of a direct contact membrane distillation system coupled to a sale-gradient solar pond for terminal lakes reclamation, Water Research, 44 (2010) 4601 - 4615.

[2] K.K. Allander, J.L. Smith and M.J. Johnson, Evapotranspiration from the lower Walker River basin, west-central Nevada, water years 2005-07: U.S. Geological Survey Scientific Investigations Report 2009-5079, 2009,

[3] M.W. Collopy and J.M. Thomas, Restoration of a desert lake in an argriculturally dominated watershed, The Walker Lake Basin, Walker Basin Project, (2010)

[4] M.W. Beutel, A.J. Horne, J.C. Roth and N.J. Barratt, Limnological effects of anthropogenic desiccation of a large, saline lake, Hydrobiologia, 466 (2001) 91 - 105.

[5] T.J. Lopes and K.K. Allander, Water budgets of the Walker River Basin and Walker Lake, California and Nevada: U.S. Geological Survey scientific investigations. Report 2009-5157, (2009)

[6] B.R. Dickerson and G.L. Vinyard, Effects of High Levels of Total Dissolved Solids in Walker Lake, Nevada, on Survival and Growth of Lahontan Cutthroat Trout, Transactions of the American Fisheries Society, 128 (1999) 507-515.

[7] T.Y. Cath, D. Adams and A.E. Childress, Experimental study of desalination using direct contact membrane distillation: a new approach to flux enhancement, Journal of Membrane Science, 228 (2004) 5 - 16.

[8] X. Wang, L. Zhang, H. Yang and H. Chen, Feasibility research of potable water production via solar-heated hollow fiber membrane distillation system, Desalination, 247 (2009) 403-411.

[9] H. Kurt, F. Halici and A.K. Binark, Solar pond conception - experimental and theoretical studies, Energy Conversion and Management, 41 (2000) 939-951.

[10] C.R. Martinetti, A.E. Childress and T.Y. Cath, High recovery of concentrated RO brines using forward osmosis and membrane distillation, Journal of Membrane Science, 331 (2009) 31-39.

[11] T. Y. Cath, D. Adams and A. E. Childress, Membrane contactor processes for wastewater reclamation in space II. Combined direct osmosis, osmotic distillation, and membrane distillation for treatment of metabolic wastewater, Journal of Membrane Science, 257 (2005) 111-119.

[12] Joshua L. Cartinella, T. Y. Cath, M. T. Flynn, Glenn C. Miller, Kenneth W. Hunter, Jr. and A. E. Childress, Removal of Natural Steroid Hormones from Wastewater Using Membrane Contactor Processes, Environmental Science & Technology, 40 (2006) 7381 - 7386.

[13] S. Al-Obaidani, E. Curcio, F. Macedonio, G. Di Profio, H. Al-Hinai and E. Drioli, Potential of membrane distillation in seawater desalination: Thermal efficiency, sensitivity study and cost estimation, Journal of Membrane Science, 323 (2008) 85-98.

[14] Z. Song, L. Li, H. Wang, B. Li and S. Wang, DCMD flux curve characteristics of cross-flow hollow fiber membrane, Desalination, (In press)

[15] M. Khayet and J. I. Mengual, Effect of salt concentration during the treatment of humic acid solutions by membrane distillation, Desalination, 168 (2004) 373-381.

[16] J. Zhang, J. Li, M. Duke, Z. Xie and S. Gray, Performance of asymmetric hollow fibre membranes in membrane distillation under various configurations and vacuum enhancement, Journal of Membrane Science, 362 (2010) 517-528.

[17] L. Mariah, C.A. Buckley, C.J. Brouckaert, E. Curcio, E. Drioli, D. Jaganyi and D. Ramjugernath, Membrane distillation of concentrated brinesâ€"Role of water activities in the evaluation of driving force, Journal of Membrane Science, 280 (2006) 937-947.

[18] J. Glater and Y. Cohen, Brine Disposal from Land-based Membrane Desalination Plants: A Critical Assessment, University of California, Los Angeles, Los Angeles, 2003,

[19] J. Cook, Passive cooling: The MIT Press, Cambridge, MA, USA, Energy Policy, 19 (1991) 83-84.

[20] C. Karim, S.M. Joma and A. Akbarzadeh, A laboratory experimental study of mixing the solar pond gradient zone, Solar Energy, 85 404-417.

[21] H. Lu, A.P. Swift, H.D. Hein Jr and J.C. Walton, Advancements in Salinity Gradient Solar Pond Technology Based on Sixteen Years of Operational Experience, Journal of Solar Energy Engineering, 126 (2004) 759-767.

[22] D.D. Weeks, S.M. Long, R.E. Emery and H.C. Bryant, What Happens when a Solar Pond Boils? In Southwest Regional Conference for Astronomy & Astrophysics, Albuquerque, New Mexico., (1981)

[23] M.R. Ramadan, A.A. El-Sebaii, S. Aboul-Enein and A.M. Khallaf, Experimental testing of a shallow solar pond with continuous heat extraction, Energy and Buildings, 36 (2004) 955-964.

[24] C. Valderrama, O. Gibert, J. Arcal, P. Solano, A. Akbarzadeh, E. Larrotcha and J. Cortina, Solar energy storage by salinity gradient solar pond: Pilot plant construction and gradient control, Desalination, 279 (2011) 445 - 450.

[25] S.S. Solis, Water desalination by membrane distillation coupled with a solar pond, Paper AAIEP05353, (1999).

[26] H. Lu, J. C. Walton and H. Hein, Thermal Desalination using MEMS and Salinity-Gradient Solar Pond Technology, 2002, UTEP, El Paso, TX.

[27] J. Walton, H. Lu, C. Turner, S. Solis and H. Hein, Solar and Waste Heat Desalination by Membrane Distillation, 2004, UTEP, El Paso, TX.

[28] R.B. Mansour, C.T. Nguyen and N. Galanis, Transient heat and mass transfer and long-term stability of a salt-gradient solar pond, Mechanics Research Communications, 33 (2006) 233-249.

[29] National Renewable Energy Laboratory (NREL), Solar Radiation Data Manual for Flat-Plate and Concentrating Collectors, 1990,

[30] M. R. Jaefarzadeh, Heat extraction from a salinity-gradient solar pond using in pond heat exchanger, Applied Thermal Engineering, 26 (2006) 1858-1865.

[31] C.A. Gueymard, The sun's total and spectral irradiance for solar energy applications and solar radiation models, Solar Energy, 76 (2004) 423-453.

[32] Francisco Suarez, Scott W. Tyler and Amy E. Childress, A fully coupled, transient double-diffusive convective model for salt-gradient solar ponds, International Journal of Heat and Mass Transfer, 53 (2010) 1718-1730.

[33] F. Suarez, A.E. Childress and S. Tyler, Temperature Evolution of an Experimental Salt-Gradient Solar Pond, Journal of Water and Climate Change, 1 (2011) 246 - 250.

[34] M.I. Ali, E.K. Summers, H.A. Arafat and J.H. Lienhard V, Effects of membrane properties on water production cost in small scale membrane distillation systems, Desalination, 306 (2012) 60-71.

[35] I. S. Bowen, The Ratio of Heat Losses by Conduction and by Evaporation from any Water Surface, Physical Review, 27 (1926) 779-787.

[36] H. Kurt, M. Ozkaymak and A.K. Binark, Experimental and numerical analysis of sodium-carbonate salt gradient solar-pond performance under simulated solar-radiation, Applied Energy, 83 (2006) 324-342.

[37] V. Alvarez, A. Baille and J. Martinez, Efficiency of shading materials in reducing evaporation from free water surfaces, Agricultural Water Management, 84 (2006) 229 - 239.

[38] S. Assouline, K. Narkis and D. Or, Evaporation suppression from water reservoirs: Efficiency considerations of partial covers, Water Resour. Res., 47 W07506.

[39] J. Wang and J. Seyed-Yagoobi, Effect Of Water Turbidity On Thermal Performance Of a Salt-Gradient Solar Pond, Solar Energy, 54 (1995) 301 - 308.

[40] M. Husain, P.S. Patil, S.R. Patil and S.K. Samdarshi, Combined effect of bottom reflectivity and water turbidity on steady state thermal efficiency of salt gradient solar pond, Energy Conversion and Management, 45 (2004) 73 - 81.

[41] N. Gasulla, Y. Yaakob, J. Leblanc, A. Akbarzadeh and J. Cortina, Brine clarity maintenance in salinity-gradient solar ponds, Solar Energy, 85 (2011) 2894 - 2902.

[42] N. Malik, A. Date, J. Leblanc, A. Azbarzadeh and B. Meehan, Monitoring and maintaining the water clarity of salinity gradient solar ponds, Solar Energy, 85 (2011) 2984 - 2996.

[43] F. Yin N. Li, W. Sun, C. Zhang, Y. Shi, Turbidity study of solar ponds utilizing seawater as salt source, Solar Energy, 84 (2010) 289 - 295.

[44] M.S. El-Bourawi, Z. Ding, R. Ma and M. Khayet, A framework for better understanding membrane distillation separation process, Journal of Membrane Science, 285 (2006) 4-29.

[45] M. Gryta, Influence of polypropylene membrane surface porosity on the performance of membrane distillation process, Journal of Membrane Science, 287 (2007) 67-78.

[46] M. Gryta, Fouling in direct contact membrane distillation process, Journal of Membrane Science, 325 (2008) 383-394.

[47] G.M. Marion, D.C. Catling, J.K. Crowley and J.S. Kargel, Modeling hot spring chemistries with applications to martian silica formation, Icarus, 212 (2011) 629-642.

[48] J.R. McCutcheon and M. Elimelech, Influence of concentrative and dilutive internal concentration polarization on flux behavior in forward osmosis, Journal of Membrane Science, 284 (2006) 237-247.

[49] C.M. Tun, A.G. Fane, J.T. Matheickal and R. Sheikholeslami, Membrane distillation crystallization of concentrated saltsâ€"flux and crystal formation, Journal of Membrane Science, 257 (2005) 144-155.

[50] W. Kleinitz, G. Dietzsch and M. Kahler, Halite Scale Formation in Gas-Producing Wells, Chemical Engineering Research and Design, 81 (2003) 352-358.

[51] G.M. Marion, J.S. Kargel and D.C. Catling, Modeling ferrous ferric iron chemistry with application to martian surface geochemistry, Geochimica et Cosmochimica Acta, 72 (2008) 242-266.

[52] G.M. Marion, CHEMCHAU Modeling Results with Walker Lake Water, Unpublished, (2012)

[53] M. Gryta, Alkaline scaling in the membrane distillation process, Desalination, 228 (2008) 128-134.

[54] E. Curcio, X. Ji, G. Di Profio, A.O. Sulaiman, E. Fontananova and E. Drioli, Membrane distillation operated at high seawater concentration factors: Role of the membrane on CaCO3 scaling in presence of humic acid, Journal of Membrane Science, 346 263-269.

[55] L.D. Nghiem and T.Y. Cath, A scaling mitigation approach during direct contact membrane distillation, Separation and Purification Technology, 80 315-322.

[56] F. He, K.K. Sirkar and J. Gilron, Effects of antiscalants to mitigate membrane scaling by direct contact membrane distillation, Journal of Membrane Science, 345 (2009) 53-58.

[57] P. Schausberger, G.M. Mustafa, G. Leslie and A. Friedl, Scaling prediction based on thermodynamic equilibrium calculation â€" scopes and limitations, Desalination, 244 (2009) 31-47.

[58] H.J. Danen-Louwerse, L. Lijklema and M. Coenraats, Coprecipitation of phosphate with calcium carbonate in Lake Veluwe, Water Research, 29 (1995) 1781-1785.

[59] T. Chen, A. Neville and M. Yuan, Influence of Mg2+ on CaCO3 formation - bulk precipitation and surface deposition, Chemical Engineering Science, 61 (2006) 5318-5327.

[60] E. Busenberg and L.N. Plummer, Kinetic and thermodynamic factors controlling the distribution of SO3 and Na in calcites and selected aragonites, Geochimica et Cosmochimica Acta, 49 (1985) 713-725.

[61] S.C. Miyasaka, J.G. Buta, R.K. Howell and C.D. Foy, Mechanism of Aluminum Tolerance in Snapbeans: Root Exudation of Citric Acid, Plant Physiology, 96 (1991) 737-743.

[62] J. Wang and J. Seyed-Yagoobi, Effects of water turbidity and salt concentration levels on penetration of solar radiation under water, Solar Energy, 52 (1994) 429 - 438.

[63] A. Rabl and C. Nielsen, Solar ponds for space heating., Solar Energy, 17 (1975) 1 - 12.

[64] F. Suárez, J.E. Aravena, M.B. Hausner, A.E. Childress and S.W. Tyler, Assessment of a vertical high-resolution distributed-temperature-sensing system in a shallow thermohaline environment., Hydrology and Earth System Sciences, 15 (2011) 1081 - 1093.

[65] Vacuum formed clear transparent balls, 2011, https://barnardltd.com/product.jsp?prodId=8127

[66] G. Gaussorgues, Infrared Thermography, Chapman and Hall, London, 1994.

[67] G. Rao, DCMD membrane modeling work, Unpublished, (2012)

[68] R.W. Schofield, A.G. Fane, C.J.D. Fell and R. Macoun, Factors affecting flux in membrane distillation, Desalination, 77 (1990) 279-294.

[69] L. Martinez and J.M. Rodriguez-Maroto, Characterization of membrane distillation modules and analysis of mass flux enhancement by channel spacers, Journal of Membrane Science, 274 (2006) 123-137.

[70] Ch. Antoine, Tension des vapeurs: nouvelle relation entre les tension et les temperatures, Comptes Rendus, 107 (1888) 681-684, 778-780, 836-837.

[71] Z. Ding, R. Ma and A.G. Fane, A new model for mass transfer in direct contact membrane distillation, Desalination, 151 (2003) 217-227.

[72] M. Qtaishat, T. Matsuura, B. Kruczek and M. Khayet, Heat and mass transfer analysis in direct contact membrane distillation, Desalination, 219 (2008) 272-292.

[73] OLI Stream Analyzer 2.0, 2005, Morris Plains, NJ.

[74] OLI Systems Inc., A Guide to Using OLI Analyzer Studio Version 3.2, (2011)

[75] T.S. Bowers and H.C. Helgeson, Calculation of the thermodynamic and geochemical consequences of nonideal mixing in the system H2O-CO2-NaCl on phase relations in geologic systems: Equation of state for H2O-CO2-NaCl fluids at high pressures and temperatures, Geochimica et Cosmochimica Acta, 47 (1983) 1247-1275.

[76] Inc. Scintag, Chapter 7: Basics of X-ray Diffraction, www.scintag.com, (1999)

[77] J.P. Schwartze and S. Bracker, The evaporation of water into air of different humidities and the inversion temperature phenomenon, International Journal of Heat and Mass Transfer, 43 (2000) 1791-1800.

[78] K. R. Cooley, Energy Relationships in the Design of Floating Covers for Evaportaion Reduction, Water Resources Research, 6 (1970) 717 - 727.

[79] S. Assouline, K. Narkis and D. Or, Evaporation suppression efficiency of partial covers: Efficiency considerations of partial covers, Water Resources Res., 47 (2011) 8.

[80] E. Sartori, A Critical Review on Equations Employed for the Calculation of the Evaporation Rate From Free Water Surfaces, Solar Energy, 68 (1999) 77 - 89.

[81] C. Hyung-Chul and J.G. Harris, Scattering of an ultrasonic beam from a curved interface, Wave Motion, 11 (1989) 383-406.

[82] F. Suarez, Salt-Gradient Solar Ponds for Renewable Energy, Desalination and Reclamation of Terminal Lakes, University of Nevada, Reno, Reno (2010).

[83] H. Lu, J.C. Walton and A.H.P. Swift, Desalination coupled with salinity-gradient solar ponds, Desalination, 136 (2001) 13-23.

[84] M. Gryta, Polyphosphates used for membrane scaling inhibition during water desalination by membrane distillation, Desalination, 285 170-176.

[85] F. He, J. Gilron, H. Lee, L. Song and K.K. Sirkar, Potential for scaling by sparingly soluble salts in crossflow DCMD, Journal of Membrane Science, 311 (2008) 68-80.

[86] M.J. Herrero, A. Martin-Parez, A.M. Alonso-Zarza, I. Gil-Peta, A. Melandez and R. Martin-Garcia, Petrography and geochemistry of the magnesites and dolostones of the Ediacaran Ibor Group (635 to 542;Ma), Western Spain: Evidences of their hydrothermal origin, Sedimentary Geology, 240 71-84.

[87] K. Xu, J. Xi, Y. Guo and S. Dong, Effects of a new modifier on the water-resistance of magnesite cement tiles, Solid State Sciences, 14 10-14.

[88] L. Martinez-Diez and M. I. Vazquez-Gonzalez, Temperature and concentration polarization in membrane distillation of aqueous salt solutions, Journal of Membrane Science, 156 (1999) 265-273.

[89] S. Hong and M. Elimelech, Chemical and physical aspects of natural organic matter (NOM) fouling of nanofiltration membranes, Journal of Membrane Science, 132 (1997) 159-181.

[90] S. Assouline, K. Narkis and D. Or, Evaporation from partially covered water surfaces, Water Resources Research, 46 (2010) 1 - 12.

[91] J.A.H. Brown, The Potential for Reducing Open Water Evaporation Losses: a Review, Hydrology and Water Resources Symposium 1988, ANU, Canberra, 1 - 3 February 1988, (1988)

[92] M.A. Garmana and M.A. Muntasserb, Sizing and thermal study of salinity gradient solar ponds connecting with the MED desalination unit, Desalination, 222 (2008) 689-695.